

AN ABSTRACT OF THE THESIS OF

Jie Ding for the degree of Master of Science in Wood Science and Engineering
presented on September 8, 2011

Title: A Methodology for Evaluating Multiple Mechanical Properties of Prototype
Microfibrillated Cellulose/Poly(lactic acid) Film Composites

Abstract approved: _____
Lech Muszynski

The context of this thesis is a research project focused on the investigation of a renewable biopolymer—poly(lactic acid) (PLA) as a potential replacement of petroleum-based polymers in advanced nanocomposites reinforced with Microfibrillated cellulose (MFC). MFC is extracted from wood, which is a renewable, sustainable, carbon neutral and recyclable material. This advanced MFC-PLA bio-based composite material is expected to allow for the substitution of petroleum-based plastics in various markets and applications.

The specific objectives of the thesis are: 1) to describe the morphological characterization of MFC used for prototype MFC-PLA composites, and 2) to determine the mechanical properties of the prototype MFC-PLA nanocomposites formulation generated in form of thin transparent films.

In order to meet this objective it was necessary to: 2.1) develop a methodology for optical strain measurement in transparent thin films; and 2.2) develop an effective methodology for obtaining multiple mechanical properties from small number of specimens of prototype materials subjected to tensile tests.

Two types of MFC, one obtained by courtesy of University of Maine and the other purchased from Innventia AB company, were investigated under a field emission scanning electron microscopy (FESEM). The micrographs obtained from FESEM showed that both types of MFC were of complex hierarchical structures, which did not allow qualitative characterization of the morphological features in terms of particulate composites nor cellular solids.

Since prototype formulations of MFC-PLA composites were generated in small amounts (typically one Petri dish) in a form of thin transparent films, there was a need for quick and efficient assessment of their key mechanical properties that would provide feedback and guide further prototyping work. An optical measurement method based on digital image correlation (DIC) principle was developed to measure the deformation and strains of the tensile film samples. In our study, the accuracy and precision of the measurement of deformation were $\pm 1.5 \mu\text{m}$ and $0.4 \mu\text{m}$ respectively. The corresponding accuracy and precision in terms of strains were $\pm 30 \mu\text{strain}$ and $75 \mu\text{strain}$ respectively. This method can be successfully used to determine the critical mechanical properties, such as elastic modulus, toughness and Poisson's ratio, of

transparent thin films by a single tensile test, all of which require precise strain measurement.

In addition, this optical measurement method makes it possible to significantly simplify the testing for measuring essential work of fracture (EWF), an important material property of thin transparent films. In traditional method, measurement of EWF requires large amount of notched specimens. However, our study showed that only a small amount of notched specimens were needed to measure the EWF of a material. This method could not be successfully used to determine EWF from un-notched tensile specimens.

©Copyright by Jie Ding

September 8, 2011

All Rights Reserved

A Methodology for Evaluating Multiple Mechanical Properties of Prototype
Microfibrillated Cellulose/Poly(lactic acid) Film Composites

by
Jie Ding

A THESIS

Submitted to

Oregon State University

in partial fulfillment of
the requirements for the
degree of

Master of Science

Presented September 8, 2011

Commencement June 2012

Master of Science thesis of Jie Ding presented on September 8, 2011.

APPROVED:

Major Professor, representing Wood Science and Engineering

Head of the Department of Wood Science and Engineering

Dean of the Graduate School

I understand that my thesis will become part of the permanent collection of Oregon State University libraries. My signature below authorizes release of my thesis to any reader upon request.

Jie Ding, Author

ACKNOWLEDGEMENTS

This project was supported by the USDA NRI Competitive Grant Program #2008-01522. I would like to express sincere appreciation to Dr. Lech Muszynski, my major professor, for his guidance, support and patience throughout this thesis project, and my co-major professor Dr. John Simonsen for his valuable advice and help. I would also like to acknowledge Milo Clauson for his guidance and help with the equipments and experiments. Gratitude must be expressed to Dr. Yi Liu and Teresa Sawyer for their help with Scanning Electron Microscopy imaging. Thank Dr. Melissa Taylor for casting MFC-PLA samples for my testing, and Dr. John Nairn for his guidance in measurement of essential work of fracture. Special thanks should be given to my colleagues Matthew Schwarzkopf, Michael Burnard, Michael Karas and Ning Guo, and all the faculty and staff in Wood Science and Engineering department. Finally, I would like to thank all of my family and friends for their help and support.

TABLE OF CONTENTS

	<u>Page</u>
1 INTRODUCTION	1
2 OBJECTIVES.....	5
2.1 Thesis Objectives.....	5
3 LITERATURE REVIEW.....	6
3.1 Microfibrillated Cellulose-Poly (Lactic Acid) Nanocomposites	6
2.2.1 Microfibrillated Cellulose (MFC).....	6
3.1.1.2 Origin of MFC	8
3.1.1.3 Properties of MFC	9
2.2.2 Poly (Lactic Acid).....	11
3.1.2.1 Definition of PLA	12
3.1.2.2 Origin of PLA.....	12
3.1.2.2 Properties of PLA.....	13
3.1.3 MFC-PLA Nanocomposites	15
3.1.4 Conclusions	16
3.2 Methods for Characterization of MFC and MFC-PLA Nanocomposites Morphology.....	17
3.2.1 Imaging techniques	17
3.2.2 Scattering techniques.....	22
3.3 Methods for Mechanical Characterization Bulk MFC-PLA Nanocomposites ..	23
3.3.1 Methods of measuring tensile propterties of MFC-PLA nanocoposite films.....	23
3.3.2 Methods of evaluating toughness.....	25
3.2.3.1 Essential work of fracture (EWF).....	26
4 MATERIALS AND METHODS.....	31
4.1 Morphological Characterization of MFC	31

TABLE OF CONTENTS (Continued)

	<u>Page</u>
4.1.1 Materials.....	31
4.1.2 Methods	31
4.1.2.1 MFC Aerogel Sample Preparation	32
4.1.2.2 Equipment	33
4.1.1.3 Procedure of FESEM Examination	33
4.1.3 Expected Output	34
4.2 Mechanical Characterization of Bulk MFC-PLA Nanocomposites.....	35
4.2.1 Materials	35
4.2.1.1 Microfibrillated Cellulose (MFC)	36
4.2.1.2 Polylactic acid (PLA) 3051D (NatureWorks®)	36
4.2.1.3 MFC-PLA nanocomposite films	36
4.2.2 Methods	38
4.2.2.1 Development of methodology of optical measurement of strains using DIC.....	39
4.2.2.2 Sample Preparation for tensile testing.....	52
4.2.2.3 Equipment	53
4.2.2.4 Procedures for mechanical tests of bulk MFC-PLA nanocomposites	53
4.2.3 Expected Output and Measured Quantities	54
4.2.4 Data Treatment	54
4.2.4.1 Tensile strength	54
4.2.4.2 Stress-strain curves	55
4.2.4.3 Elastic modulus	59
4.2.4.4 Toughness.....	59

TABLE OF CONTENTS (Continued)

	<u>Page</u>
4.3 Developing an Alternative Method of Evaluating Essential Work of Fracture (a proof of concept).....	62
4.3.1 Materials	62
4.3.2 Methods	64
4.3.2.1 Theory of EWF calculation using DIC	64
4.3.3 Expected Output and Measured Quantities	72
4.3.4 Data Treatment	72
4.3.4.1 EWF calculated from traditional experimental method	73
4.3.4.2 EWF calculated from method based on optical measurement using DIC.....	73
4.3.5 Verification of the alternative method of EWF measurement	73
4.3.5.1 EWF measured using traditional method	74
4.3.5.2 EWF measured using optical measurement	76
5. RESULTS AND DISCUSSION	78
5.1 Morphological characterization of MFC.....	78
5.2 Mechanical characterization of bulk MFC-PLA nanocomposites.....	84
5.2.3 Mechanical properties of MFC-PLA nanocomposite films.....	84
6 CONCLUSIONS	92
BIBLIOGRAPHY.....	94
APPENDICES	99
Appendix A: DIC Setup and Working Procedures.....	100
Appendix B—Equivalence of Equations (9) and Equation (10)	106
Appendix C—Matlab Codes for EWF Computation	109
Appendix D—SEM Micrographs of MFC Aerogel Samples.....	112

LIST OF FIGURES

<u>Figure</u>	<u>Page</u>
Figure 1. Biopolymers global production from year 2007 to 2010 (PolyOne 2008)	2
Figure 2. Structure and appearance of MFC by SEM: a) micro-scale ; and b) nano-scale (Cheng and Wang 2008).....	10
Figure 3 AFM images of MFC on mica after drying (Paakko, Ankerfors et al. 2007)....	10
Figure 4. Synthesis methods for high-molecular-weight PLA (Garlotta 2001).....	13
Figure 5. NatureWorks® PLA Pellets (Gerlock 2011)	14
Figure 6. Cast MFC-PLA nanocomposites film.....	23
Figure 7. Specimen geometry for double-edge notched tensile (DENT) specimens. ..	27
Figure 8. Schematic drawing of the relationship between specific total work to failure w_t and ligament length l . Black dots are typical experimental data points (Liu and Nairn 1998).....	29
Figure 9. (a) original MFC suspension; (b) freeze-dried MFC aerogel after freeze drying	32
Figure 10. Setup of tensile testing on transparent films employing optical measurement of deformation based on DIC principle.	40
Figure 11. Accuracy and precision assessment for an individual specimen: (a) horizontal displacement error (u); (b) vertical displacement error (v);	43
Figure 12. Accuracy and precision assessment for each specimen: (a) horizontal displacement error (u); (b) vertical displacement error (v); (c) horizontal strain error (ϵ_{xx}); (d) vertical strain error (ϵ_{yy}).....	45
Figure 13. overall accuracy and precision assessment: (a) accuracy of displacement; (b) precision of displacements; (c) accuracy of strain; (d) precision of strains	46

LIST OF FIGURES (Continued)

<u>Figure</u>	<u>Page</u>
Figure 14 Eight different printed speckle patterns: Pr01 and Pr02 with uniform gray scale but different gray scale levels; Pr03-Pr06 with regular speckle patterns but different spacing; Pr07 (Gallery 2011) and Pr08 with random speckle patterns	48
Figure 15. Accuracy and precision of displacement in horizontal direction for all patterns	49
Figure 16. Accuracy and precision of displacement in vertical direction for all patterns	49
Figure 17. Accuracy and precision of strain in horizontal direction for all patterns	50
Figure 18. Accuracy and precision of strain in vertical direction for all patterns	50
Figure 19. Specimens for tensile testing before and after applying random speckles	52
Figure 20. Four methods of strain calculation: a) means strain over the AOI; b) mean strain within plastic deformation zone; c) based on virtual extensometer; d) based on Instron crosshead movement	57
Figure 21. Typical stress-strain curves generated using four different approaches ...	58
Figure 22. Typical plot of an absolute value of the horizontal strain vs. vertical strain curve for MFC-PLA film samples	61
Figure 23. Three types of deformation in a DENT sample in tension: case 1, elastic deformation for points far away from the ligament; case 2, plastic deformation for points within the plastic deformation zone; case 3, plastic deformation and fracture for points along the ligament.....	65
Figure 24. Left: Typical strain map of a DENT specimen just before failure; Right: nominal stress vs. local strain curves at location a (within plastic deformation zone) and b (elastic deformation zone)	66
Figure 25. Strain mapping of a specimen after failure.....	67
Figure 26. Typical stress-strain curve for a point A_j	68

LIST OF FIGURES (Continued)

<u>Figure</u>	<u>Page</u>
Figure 27. Typical load-displacement curves for all the seven ligament-length groups	74
Figure 28. Specific work to failure wf as a function of ligament length l	75
Figure 29 Comparison of EWF measured using optical measurement for three groups of DENT specimens.....	76
Figure 30. Microstructure of a dry sponge swab (Carr 2007)	79
Figure 31. Structure and appearance of MFC by SEM a) type A MFC, 20 000X; b) type B MFC, 20 000X; c) type A MFC, 50 000X; d) type B MFC, 50 000X	80
Figure 32. SEM micrographs of type A MFC aerogel at different levels of magnification: (a) 100 X; (b) 1500X; (c) 6500 X (d)50,000 X	81
Figure 33. SEM micrographs of type B MFC aerogel at different levels of magnification: (a) 1000 X; (b) 10,000X; (c) 65,000 X (d) 200,000 X	82
Figure 34. Tensile strength as a function of type A MFC loading levels for (by weight) MFC-PLA nanocomposite films with untreated MFC and lactide treated MFC	85
Figure 35. Elastic modulus as a function of type A MFC loading levels (by weight) for MFC-PLA nanocomposite films with untreated MFC and lactide treated MFC	86
Figure 36. Toughness as a function of type A MFC loading levels (by weight) for MFC- PLA nanocomposite films with untreated MFC and lactide treated MFC.....	86
Figure 37. Tensile strength as a function of type B MFC loading levels (by weight) for MFC-PLA nanocomposite films with untreated MFC and lactide treated MFC	88
Figure 38. Elastic modulus as a function of type B MFC loading levels (by weight) for MFC-PLA nanocomposite films with untreated MFC and lactide treated MFC	89

LIST OF FIGURES (Continued)

<u>Figure</u>	<u>Page</u>
Figure 39. Toughness as a function of type B MFC loading levels (by weight) for MFC-PLA nanocomposite films with untreated MFC and lactide treated MFC.....	89

LIST OF TABLES

<u>Table</u>	<u>Page</u>
Table 1. Terminologies and dimensions related to cellulose units from plants (Beck-Candanedo, Roman et al. 2005; Wu, Henriksson et al. 2007; Sehaqui, Allais et al. 2010; Siró and Plackett 2010)	7
Table 2. Tensile strengths and moduli of engineering materials compared to cellulose (Oksman, Mathew et al. 2006; Eichhorn, Dufresne et al. 2010; MatWeb 2011)	11
Table 3. Mechanical properties of PLA polymer and other common polymers (Kroschwitz 1990).....	15
Table 4. SEM imaging examples for MFC, other cellulose nanoparticles and their nanocomposites in the literature.....	19
Table 5. TEM imaging examples for MFC, other cellulose nanoparticles and their nanocomposites in the literature.....	20
Table 6. AFM imaging examples for MFC, other cellulose nanoparticles and their nanocomposites in the literature.....	21
Table 7. Numbers of specimens with type A MFC	38
Table 8. Numbers of specimens with type B MFC.....	38
Table 9. Ligament length and number of specimens tested for measurement of EWF	63
Table 10. EWF measured from three groups of DENT specimens and determined by John Nairn's Method.....	77
Table 11. Tensile strength, elastic modulus, toughness and Poisson's ratio of MFC-PLA nanocomposites with type A MFC	85
Table 12. Tensile strength, elastic modulus, toughness and Poisson's ratio of MFC-PLA nanocomposites with type B MFC	88

A Methodology for Evaluating Multiple Mechanical Properties of Prototype Microfibrillated Cellulose/Poly(lactic acid) Film Composites

1 INTRODUCTION

Long-term economical sustainability of nations depends on the finding and utilizing viable renewable alternatives to non-renewable raw materials and fossil fuels like petroleum. To date, most conventional polymers (polyethylene, polypropylene, polyvinyl chloride, polystyrene, etc.) are petroleum-based. They are usually associated with lower production costs and higher mechanical properties compared to renewable, non-petroleum based biopolymers (PolyOne 2008). The key for replacing petroleum-based polymers with renewable biopolymers is the ability to combine cost-effective production with competitive mechanical properties.

Poly(lactic acid) (PLA) is one of the few commercially available biopolymers which has similar properties to those of petroleum-based plastics (Siró and Plackett 2010). It is a versatile polymer derived from renewable agricultural raw materials and shows great potential for applications in packaging and the automotive and biomedical fields (Mathew, Oksman et al. 2005; Liu, Yuan et al. 2010). Low cost PLA products have been widely used in many applications, including packaging films, thermoformed containers and bottles. As a cost-competitive alternative to petroleum-based plastics, PLA products will help lessen dependency on volatile petroleum-based feedstocks (Glasbrenner 2005). The annual rate of increase in the worldwide production capacity of PLA was ~100

million lbs/year in 2007, and expanded to over 1000 million lbs/year in 2010. Figure 1 shows the global production of major biopolymers from year 2007 to 2010.

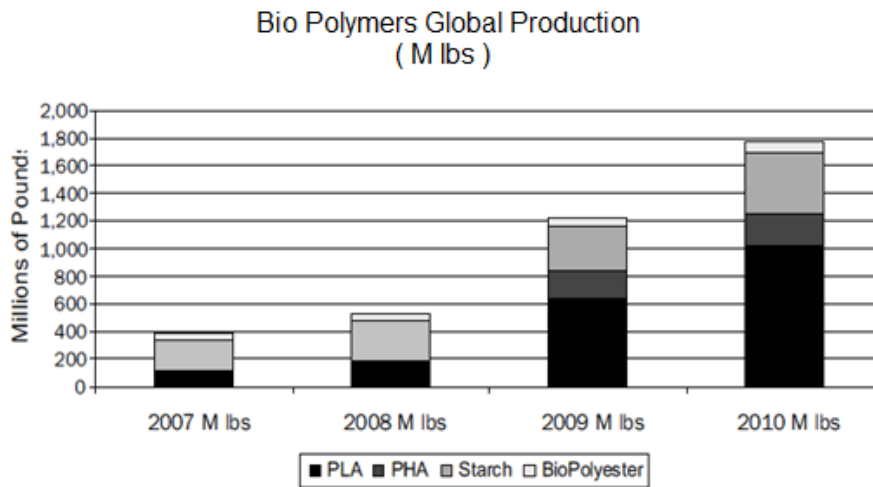


Figure 1. Biopolymers global production from year 2007 to 2010 (PolyOne 2008)

From the perspective of mechanical performance, a recent trend is to reinforce biopolymers by adding nanofillers (Pettersson and Oksman 2006; Hubbe and Rojas 2008; Eichhorn, Dufresne et al. 2010). Studies show that tensile strength, the elastic modulus and the storage modulus of PLA can be dramatically increased by adding nanofiber fillers (Mathew, Oksman et al. 2005; Ikeda, Takatani et al. 2008; Iwatake, Nogi et al. 2008).

One desirable candidate of such nano-fillers is microfibrillated cellulose (MFC), which has a high aspect ratio (100-150) nano-scale fibrous network structure, is extracted from

wood and is a renewable, sustainable, carbon neutral and recyclable material (Siró and Plackett 2010). Recently in Europe, a new production process for MFC has been developed, which is expected to drastically lower the price of this product and make it cost competitive for the envisioned commercial uses (Lindström, Ankerfors et al. 2007). However, experimental results to date reported in the literature to-date show that the addition of cellulose nanofiber decrease the toughness of neat polymer matrix (Ikeda, Takatani et al. 2008; Iwatake, Nogi et al. 2008; Menezes, Siqueira et al. 2009).

The larger context for this thesis is a USDA funded project. The overall objective of this project is to develop high-performance bio-nanocomposites from Microfibrillated Cellulose (MFC) and Poly(lactic acid) (PLA) by optimizing the coupling agent. Morphological characterization of MFC and mechanical characterization of MFC and MFC-PLA composites help in understanding the structure-property relationships between the components, the role of surface chemistry in modifying the nature of the filler-matrix interphase, and the stiffness-toughness combinations of these nanocomposites.

The specific objectives of the thesis are: 1) to describe the morphological characteristics of MFC, and 2) to determine the mechanical properties of MFC-PLA nanocomposite films.

Many formulations of MFC-PLA composites were generated in the search of "the perfect

one". While prototype formulations of MFC-PLA composites are generated in small amounts (typically one Petri dish) in a form of thin transparent films, there is a need for quick and efficient assessment of their key mechanical properties that would provide feedback and guide further prototyping work. Ideally, the critical mechanical properties including elastic modulus, tensile strength, Poisson ratios, and toughness would be obtained from the small amount of the prototype material generated in a trial. The problem is that strains of thin film samples cannot be easily measured by conventional methods (strain gauge or extensometer), which interfere with the measurement due to their stiffness (strain gauge) or weight (extensometers). Therefore, an optical measurement method based on digital image correlation (DIC) principle was introduced to measure the deformation and strains of the tensile film samples. However, since the film samples are transparent, it is hard to separate the specimen surface from its background. This could be a big challenge for optical measurement of deformation and strains. Solutions for this challenge will be discussed in the thesis.

2 OBJECTIVES

2.1 Thesis Objectives

The objectives of this thesis are:

1. To characterize the morphology of Microfibrillated Cellulose (MFC) used for prototype MFC-PLA composites and their network structures.
2. To determine the mechanical properties of the prototype bulk MFC-PLA nanocomposites formulations generated in form of transparent thin films, and pure PLA matrix as reference. The mechanical properties of interest include tensile strength, modulus of elasticity, toughness and Poisson's ratio.

In order to meet this objective, it was necessary to:

- 2.1 develop a methodology for optical strain measurement in transparent thin films
- 2.2 develop an effective methodology for obtaining multiple mechanical properties from small number of specimens of prototype materials subjected to tensile tests.

3 LITERATURE REVIEW

3.1 Microfibrillated Cellulose-Poly (Lactic Acid) Nanocomposites

Generally, nanocomposites are two-phase materials, in which one of the phases has at least one dimension in the nanometer range (1-100 nm) (Siró and Plackett 2010). The two major components in nanocomposites investigated in this study are microfibrillated cellulose and poly(lactic acid). In this section, definition, origin and known properties including morphological and mechanical properties of MFC and PLA will be discussed. Recent studies on MFC-PLA nanocomposites will also be summarized in this section.

2.2.1 Microfibrillated Cellulose (MFC)

Cellulose is one of the most abundant biopolymers on the earth. It can be derived from wood, cotton, hemp and other plant-based materials. The cellulose nanofibril from wood and its application in nanocomposite materials have gained increasing attention due to the high strength and high stiffness of the cellulose crystals (Siró and Plackett 2010).

3.1.1.1 Definition of MFC

The term “microfibrillated cellulose” (MFC) refers to cellulosic fibrils disintegrated from the plant cell walls (Svagan, Samir et al. 2007). The thickness of MFC could be as small as 3-10 nm, but is typically in the range of 20-40 nm because of aggregation of cellulose microfibrils (Svagan, Samir et al. 2007). The length is typically in the order of

micrometer scale. Synonyms for MFC used in the literature included cellulose nanowhiskers (CNWs) (Petersson and Oksman 2006; Kvien and Okaman 2007; Braun, Dorgan et al. 2008), nanocellulose (Sun-Young, Mohan et al. 2009), cellulose whiskers (Kvien and Tanem 2005), nanofiber, whiskers, nanorods, rod-like cellulose microcrystals, nanowires and nanofibrillar cellulose (NFC) (Hubbe and Rojas 2008). Although these terminologies above refer to nanoscale fibers, the fibers are slightly different in diameters. Table 1 summarizes the terms and dimensions related to sub-micron cellulose units from plants used in the literature.

Table 1. Terminologies and dimensions related to cellulose units from plants (Beck-Candanedo, Roman et al. 2005; Wu, Henriksson et al. 2007; Sehaqui, Allais et al. 2010; Siró and Plackett 2010)

Term	Diameter (nm)	Length (nm)	Aspect Ratio (L/d)
Cellulose microfibrils	2-10	>10,000	>1000
Microcrystalline cellulose (MCC)	15-30 when aggregated	200-400	~10
Cellulose nanocrystals (CNC)	3-5	100-300	20-100
Cellulose whiskers	2-20	100-600	10-100
Microfibrillated cellulose (MFC)	25-100	>1000	100-150

In this thesis, we are primarily concerned with MFC due to their superior aspect ratio.

3.1.1.2 Origin of MFC

MFC can be obtained from almost any cellulosic material such as beet pulp, potato tuber cells, wheat straw, tunicin, crab shell chitin and bacterial cellulose (Hubbe and Rojas 2008). Among these biomaterials, wood has been considered as an attractive source for production of MFC due to its great abundance (Oksman and Sain 2006; Hubbe and Rojas 2008).

To isolate MFC from wood, multi-stage process is required, involving chemical delignification (pulping and bleaching), mechanical diminution and chemical diminution. These processes are often used sequentially or in combination (Hubbe and Rojas 2008).

The purpose of chemical delignification is to remove lignin, which connects microfibers together. This process is considered as a promising initial step for the preparation of nanocellulose materials (Moran, Alvarez et al. 2008). If colorless cellulosic nanomaterials and a high degree of crystallinity are desired, bleaching treatments are required to allow any dissolved lignin or carbohydrate byproducts to be incinerated, with the recovery of energy in the delignification process (Hubbe and Rojas 2008). Mechanical diminution provides extensive separation of bleached fibers into nano-sized fibrils. Conventional approach of refining is to pass the fibers between rotating and stationary discs or cones having patterns of raised rectangular bars, separated by groove spaces (Hubbe and Rojas 2008). Another approach of breaking fibers down to nano-sized fibrils is to pass the material through a small nozzle at very high pressure. This approach is often used in

combination with other treatment (Nakagaito and Yano 2004).

Chemical diminution treatments are almost always combined with the mechanical diminution treatments (Hubbe and Rojas 2008). Acid hydrolysis and enzymatic treatment are two major methods for breaking down the amorphous cellulose and liberating cellulosic nano-sized crystals into suspension (Henriksson, Henriksson et al. 2007; Elazzouzi-Hafraoui, Nishiyama et al. 2008).

3.1.1.3 Properties of MFC

- Morphological description

Techniques such as transmission electron microscopy (TEM), scanning electron microscopy (SEM), atomic force microscopy (AFM) and wide-angle X-ray scattering (WAXS) have been widely used to characterize MFC morphology. Although these methods can provide information on MFC widths, it is hard to determine MFC lengths due to entanglements. Both ends of individual MFC are very difficult to identify (Siró and Plackett 2010). Many studies show that MFC are usually in the form of nanofiber aggregates due to the high density of hydroxyl groups on the microfibril surface, which can strongly interact and lead to aggregation (Zimmermann, Pohler et al. 2004; Andresen, Johansson et al. 2006; Zimmermann, PÖHLER et al. 2006). Examples of SEM and AFM images of MFC are showed in Figure 2 and Figure 3 respectively.

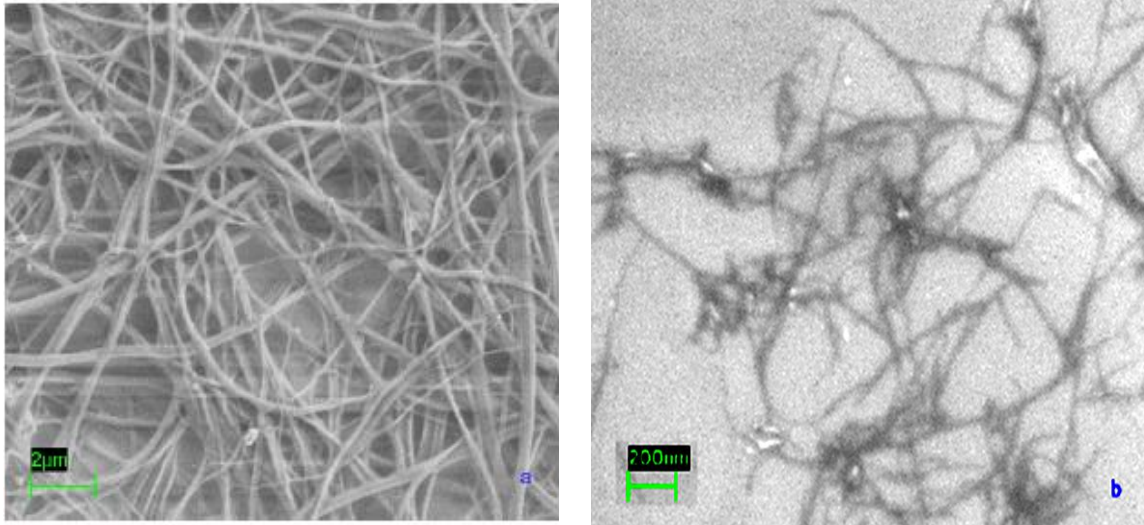


Figure 2. Structure and appearance of MFC by SEM: a) micro-scale ; and b) nano-scale (Cheng and Wang 2008)

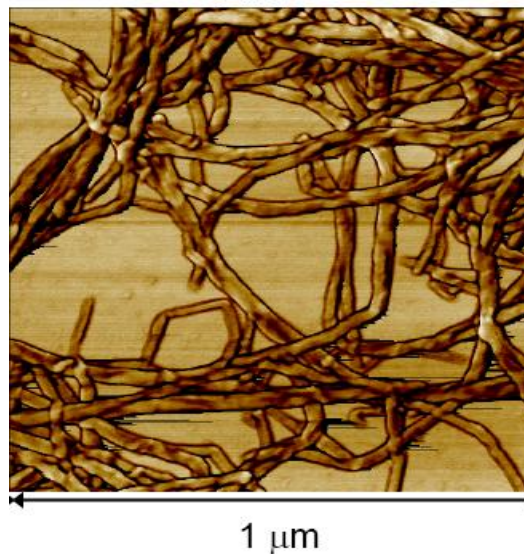


Figure 3 AFM images of MFC on mica after drying (Paakko, Ankerfors et al. 2007)

- Mechanical Properties

MFC is expected to have very high Young's modulus since the Young's modulus of cellulose crystal is as high as 134 GPa (Oksman and Sain 2006). The tensile strength of cellulose crystals was estimated to be between 0.8 and 10 GPa (Nishino, Takano

et al. 1995). The comparisons of tensile strengths and moduli for crystalline cellulose and a number of common engineering materials are list in Table 2.

Table 2. Tensile strengths and moduli of engineering materials compared to cellulose (Oksman, Mathew et al. 2006; Eichhorn, Dufresne et al. 2010; MatWeb 2011)

Material	Tensile Strength (MPa)	Modulus (GPa)	Density (g/cm ³)
Aluminum	90	69	2.7
Steel	450-1950	200	7.8
Glass	3300	69	2.5
Crystalline cellulose	10,000	138	1.5

The high values of tensile strength and modulus, combined with the low density of crystalline cellulose allow MFC to be an attractive reinforcement for polymers.

2.2.2 Poly (Lactic Acid)

Poly(lactic acid), or PLA is one of the few commercially available biopolymers. It has similar properties to those of petroleum-based plastics such as polyethylene and polypropylene (Momani 2009; Siró and Plackett 2010). PLA has been used as packaging, disposable cups, plates and containers, plastic bags, barriers for sanitary products and diapers, and medical applications such as implants, nails and screws for surgery (Mathew, Oksman et al. 2005; Momani 2009; Liu, Yuan et al. 2010).

3.1.2.1 Definition of PLA

PLA is a versatile thermoplastic polymer derived from renewable agricultural raw materials (e.g. corn, wood residues or other biomass). It belongs to the family of aliphatic polyesters commonly made from α -hydroxy acids (Garlotta 2001). PLA is ultimately degradable under composting conditions, so that as it is decomposed by micro-organisms, all of it eventually is recycled back to carbon dioxide in the atmosphere (Mathew, Oksman et al. 2005; Braun, Dorgan et al. 2006; Siró and Plackett 2010)

3.1.2.2 Origin of PLA

The basic repeating unit of PLA is lactic acid, which was first isolated in 1780 from sour milk and first produced commercially in 1881 (Hartmann 1998). Lactic acid is the simplest hydroxyl acid with an asymmetric carbon atom and exists in two optically active configurations. The chemical structure of lactic acid is shown in Figure 4.

There are mainly three routes of polymerization to synthesize lactic acid into PLA of high degree of polymerization, as illustrated in Figure 4. The first route is that lactic acid is condensation polymerized to yield a low-molecular-weight polymer followed by increasing molecular weight by introducing chain-coupling agents. The second route is to collect, purify, and ring-open polymerize (ROP) lactide to produce high-molecular-weight PLA. The ring-open polymerization of lactide method was the only method of producing pure PLA of high molecular weight until Mitsui Toatsu Chemicals

commercialized a process wherein lactic acid and catalyst are dehydrated in a high-boiling solvent under reduced pressures to yield high -molecular-weight PLA (Garlotta 2001).

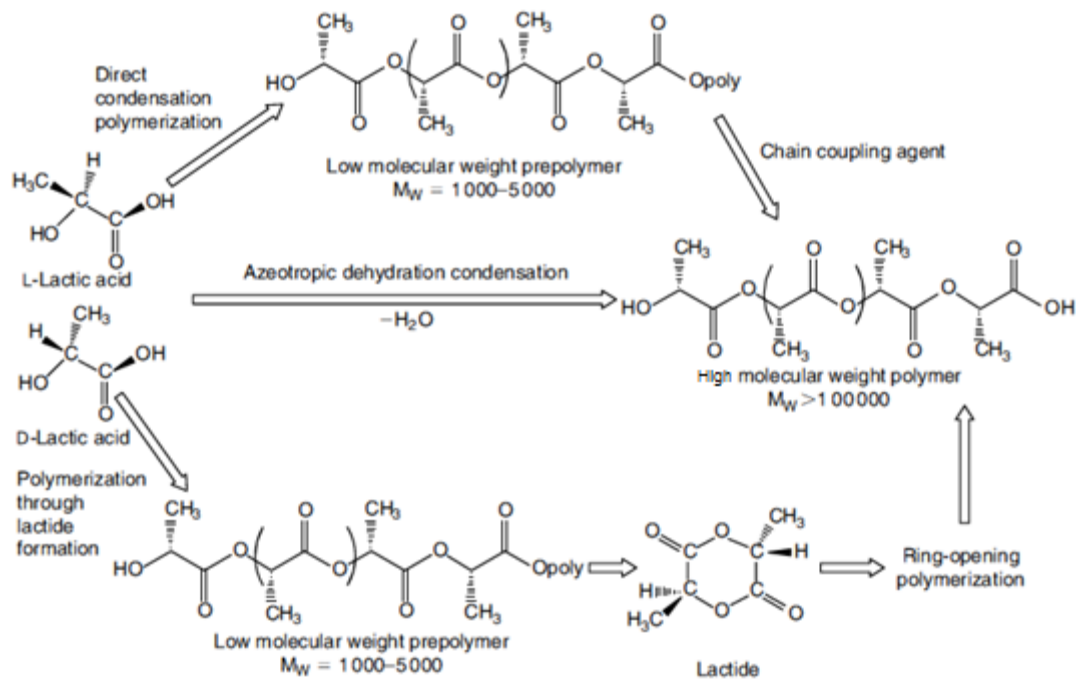


Figure 4. Synthesis methods for high-molecular-weight PLA (Garlotta 2001)

3.1.2.2 Properties of PLA

- Physical properties

High-molecular-weight PLA is a colorless, glossy, stiff thermoplastic polymer. It has a glass transition temperature of about $55\text{ }^{\circ}\text{C}$ and a melt temperature of about $175\text{ }^{\circ}\text{C}$ (Garlotta 2001). The solid amorphous PLA density is $\sim 1.25\text{ g/cm}^3$, and the pure crystalline PLA density is estimated to be $1.37-1.49\text{ g/cm}^3$ (Witzke 1997). Figure 5

shows the commercial PLA pellets from NatureWorks® LLC which is one of the major company producing PLA products in the world.



Figure 5. NatureWorks® PLA Pellets (Gerlock 2011)

- Mechanical properties

PLA has relative good toughness and strength compared to commonly used petroleum-based plastics. However, the main drawback of PLA in mechanical properties is its inherent brittleness. Although numerous approaches such as plasticization, block copolymerization, and blending with tough polymers have been adopted to improve the toughness of brittle PLA, these methods significantly decrease the strength and modulus of PLA (Martin and Averous 2001; Lemmouchi, Perry et al. 2007). Most research on PLA composites ultimately seeks to improve the material properties to a level with good stiffness-toughness balance, which satisfies a particular application. Mechanical Properties of PLA and two commonly used polymers, polyethylene terephthalate (PET)

and polypropylene (PP), are summarized in Table 3.

Table 3. Mechanical properties of PLA polymer and other common polymers (Kroschwitz 1990)

Property	Polyethylene Terephthalate (PET)	Polypropylene (PP)	PLA* (NatureWorks®)
Tensile Yield Strength (MPa)	81	35	48
Flexural Modulus (GPa)	3	1.8	3.83
Elongation at yield (%)	4	12	2.5

* PLA properties were provided from NatureWorks®PLA 3051D technical data sheets

3.1.3 MFC-PLA Nanocomposites

Nanocomposite in general is a two-phase material where one of the phases has at least one dimension in nanometer range (1-100 nm). Compared with conventional composites, nanocomposites have superior thermal, mechanical and barrier properties at low reinforcement levels (e.g., ≤ 5 wt%), and also better recyclability and transparency (Oksman, Mathew et al. 2006). Due to their abundance, biodegradability and high performance of mechanical properties, cellulose nanofibrils, such as MFC, become excellent reinforcement for PLA. Studies have shown that an addition of MFC significantly improves the tensile strength and elastic modulus of PLA (Iwatake, Nogi et al. 2008). In the study by Iwatake et al. a 10 % MFC load (by weight) resulted in elastic modulus increase of 40% and strength gains of 25% over the neat PLA. In addition, MFC in PLA polymer matrix help reduce gas permeability because the presence of the crystalline fibers increases the travel path for gas movement through the composite (Lagaron, Catala et al. 2004).

The potential improvement of fiber-reinforced composites depend on many factors, including degree of dispersion, fiber/matrix adhesion, fiber content, fiber size and fiber aspect ratio (Dufresne, Dupeyre et al. 2003; Mathew, Oksman et al. 2005). In order to deliver good dispersion of MFC in PLA, an organic solvent (e.g. acetone) is used to replace the water in MFC, and subsequently MFC is mixed with PLA previously dissolved in the same solvent. Then thin films can be obtained by compression molding of the compounds after removal of the solvent by evaporation (Iwatake, Nogi et al. 2008).

3.1.4 Conclusions

Since both MFC and PLA are derived from renewable material and both are environmentally friendly, MFC-PLA nanocomposites are fully bioresource-based, sustainable "green-composites". Many studies on fabrication of MFC-PLA nanocomposites have showed mechanical properties of PLA, such as tensile strength, elastic modulus and storage modulus can be improved by introducing MFC as reinforcement (Iwatake, Nogi et al. 2008; Suryanegara, Nakagaito et al. 2009). Therefore, there is a great potential of MFC-PLA nanocomposites to substitute petroleum-based plastics in a variety of applications. However, to date, no evidence that tensile strength, elastic modulus and toughness of PLA could be improved at the same time by adding either MFC or other types of cellulose nanofibrils was found in the literature. One of the objectives of our project is to increase the toughness of PLA by the introduction of MFC without substantial decrease of strength and modulus.

3.2 Methods for Characterization of MFC and MFC-PLA Nanocomposites Morphology

In fiber-reinforced composites, morphological characteristics of reinforcement such as fiber size and aspect ratio influence the mechanical properties of the composites (Dufresne, Dupeyre et al. 2003). To better understand the structure-property relationship between the components of MFC-PLA nanocomposites, it is necessary to investigate the morphological characteristics of MFC and information about dispersion of MFC in PLA matrix.

Various techniques have been used to investigate morphological characteristics of cellulose nanofibrils and nanocomposites. These techniques can be categorized into two types: imaging techniques and scattering techniques.

3.2.1 Imaging techniques

The most common methods used to obtain information about the shape and size of cellulosic nanoparticles and particle distribution in matrix are scanning electron microscopy (SEM), transmission electron microscopy (TEM), and atomic force microscopy (AFM) (Kvien and Tanem 2005; Hubbe and Rojas 2008). The features of these methods and examples of investigating morphological characteristics of cellulose nanofibrils list as follows:

- a) Scanning Electron Microscopy (SEM) and Field emission scanning electron microscopy (FESEM)

SEM, including FESEM, is a convenient method to investigate morphology of MFC and

MFC distribution in the composites. It allows for a quick examination giving an overview of the sample. It can be used to verify the presence of possible larger aggregates in the composites. (Kvien et al. 2005).

SEM in general has lower resolution when compared to TEM. Typically, the resolution of SEM is 1-2 nm, and the resolution of TEM can be up to less than 0.1 nm. In addition, MFC samples require coating treatment due to their nonconductivity. SEM imaging examples for MFC, other cellulose nanoparticles and their nanocomposites in the literature are listed in Table 4. The scale of image quality is none, poor, no good (NG), OK/satisfactory, good and excellent based on the feasibility of image analysis.

Table 4. SEM imaging examples for MFC, other cellulose nanoparticles and their nanocomposites in the literature

Type	Mode	Applied Voltage	Image Quality	Resolution	Literature Source
FESEM	Hitachi S-4300	20 KV	OK	1.5 nm @15KV	(Kvien and Tanem 2005)
FESEM	Hitachi S-4300	10 KV	OK (composite)	5.0 nm @ 1 KV	(Kvien and Tanem 2005)
FESEM	JEOL JSM-7000F	1.5 KV	Good	1.2 nm @30KV 1.5 nm @15KV 3.0 nm @ 1 KV	(Braun, Dorgan et al. 2008)
SEM	LEO 1525	5 KV	OK	1.5 nm @ 20 KV	(Juntaro, Pommet et al. 2007)
SEM	JEOL JSM-5300	30 KV	OK (composite)	4.0 nm @ 30 KV	(Juntaro, Pommet et al. 2007)
SEM	JEOL 6310	10 and 15 KV	OK	2.5 nm	(Sun-Young, Mohan et al. 2009)
FESEM	Hitachi S-4300	5 KV	OK (composite)	1.5 nm @15KV 5.0 nm @ 1 KV	(Kvien and Okaman 2007)
FESEM	Hitachi S-4300	5 KV	OK	1.5 nm @15KV 5.0 nm @ 1 KV	(Pettersson, Kvien et al. 2007)

b) Transmission electron microscopy (TEM)

TEM typically has a higher resolution than SEM. The tendency of agglomeration of nano-sized fibers can be observed with TEM. In addition, it is possible to employ TEM to identify individual cellulose nanofibrils, which enable determination of their sizes, shape and aggregated state of the nanofibrils.

However, TEM analysis of the nanocomposites structure is challenging for several reasons. The major problem is lack of contrast between MFC and PLA matrix. Staining treatment may be needed to enhance the contrast (Kvien and Tanem 2005). TEM imaging examples for MFC, other cellulose nanoparticles and their nanocomposites in the literature are listed in Table 5. The scale of image quality is none, poor, no good (NG), OK/satisfactory, good and excellent based on the feasibility of image analysis.

Table 5. TEM imaging examples for MFC, other cellulose nanoparticles and their nanocomposites in the literature

Mode	Applied Voltage	Image Quality	Resolution	Literature Source
Philips CM 30	150 KV	Good (stained*), NG for composites	0.23 nm	(Kvien and Tanem 2005)
Philips CM 200	200 KV	OK (stained*)	0.19 nm	(Braun, Dorgan et al. 2008)
Philips CM 200	80 KV	Good (stained*)	0.19 nm	(Elazzouzi-Hafraoui, Nishiyama et al. 2008)
Philips CM 30	100 KV	Good (stained*), OK for composite	0.23 nm	(Petersson and Oksman 2006)

*Samples were stained by allowing the grids to float in a 2 wt% uranyl acetate for 2-3 min

c) Atomic force microscopy (AFM)

AFM is a good alternative to electron microscopy for analysis of surface morphology of MFC and MFC nanocomposites, without any limitations regarding contrast and resolution. Resolution of AFM directly depends on the resolution of the probes. However, AFM may overestimate the width of the whiskers due to the tip-broadening effect (Kvien

and Tanem 2005). AFM imaging examples for MFC, other cellulose nanoparticles and their nanocomposites in the literature are listed in Table 5. The scale of image quality is none, poor, no good (NG), OK/satisfactory, good and excellent based on the feasibility of image analysis.

Table 6. AFM imaging examples for MFC, other cellulose nanoparticles and their nanocomposites in the literature

Mode	Applied Tip	Effect	Literature Source
NanoScope IIIa, multimode SPM from Veeco	Si Nanoprobes SPM tips	Good	(Kvien and Tanem 2005)
NanoScope IIIa, multimode SPM from Veeco	Si Nanoprobes SPM tips	Good OK for composite*	(Kvien and Okaman 2007)
Molecular Imaging PicoPlus	Micromash NC36 tip	OK	(Elazzouzi-Hafraoui, Nishiyama et al. 2008)

*Composite samples were etched with ionized argon gas to remove the soft polymer from the surface. The etched time was 90 min (3 KV, 1 mA).

3.2.2 Scattering techniques

Scattering techniques are powerful methods for the characterization of particles. They can provide quick, easy, and reproducible measurements of particles with a wide range of size (<0.05-10,000 μm) (Selomulya 2001). Among them, light scattering and X-ray scattering are two major scattering techniques.

Multi-angle laser-light scattering is an established technique, which has been extensively used for the analysis of particles in various media. It allows determining the physical properties of nanoparticles such as size, shape and molecular weight (Braun, Dorgan et al. 2008).

(Elazzouzi-Hafraoui, Nishiyama et al. 2008) used wide-angle X-ray scattering (WAXS) to investigate the orientation and size of the elementary crystallites of cotton cellulose whiskers, and also used small-angle X-ray scattering (SAXS) to simulate the profiles of cellulose whisker, combining the dimensions and size distribution functions determined by TEM and AFM.

3.3 Methods for Mechanical Characterization Bulk MFC-PLA Nanocomposites

MFC-PLA nanocomposites produced by casting with low loading levels of MFC (≤ 5 wt%) are typically in the form of transparent thin films. Figure 6 shows an MFC-PLA film sample cast in a Petri dish. It is expected that critical mechanical properties, such as tensile strength, elastic modulus and toughness of MFC-PLA nanocomposite films, like the sample show in Figure 6 are quickly determined to guide development of further prototype formulations.

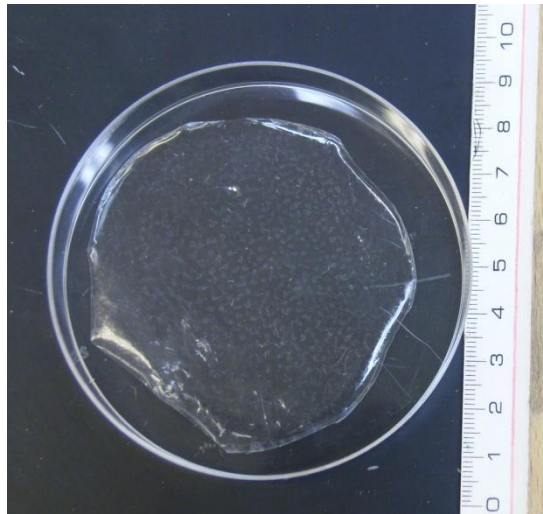


Figure 6. Cast MFC-PLA nanocomposites film

3.3.1 Methods of measuring tensile properties of MFC-PLA nanocomposite films

Following are several ASTM standards to which one can refer for mechanical testing on polymeric film samples:

- ASTM D3039: Standard Test Method for Tensile Properties of Polymer Matrix

Composite Materials.

- ASTM D882: Standard Test Method for Tensile Properties of Thin Plastic Sheeting.
- ASTM D638: Standard Test Method for Tensile Properties of Plastics.

Since the common devices (strain gauges or extensometers) for direct measurement of specimen deformation cannot be effectively used on thin films, these standards recommend that, for tensile modulus of elasticity determinations, a specimen gage length of 250 mm shall be considered as standard in order to minimize the effects of grip slippage on test results. However, this length is not feasible for specimens cut from cast samples produced in Petri dishes. In general, an MFC-PLA composite film sample cast in a Petri dish is about 80 mm in diameter. Therefore, the lengths of tensile testing specimens cut from the film sample are usually less than 70 mm.

Some researchers modified the ASTM standards on specimen size due to the limited size of samples available. For instance, (Juntaro, Pommet et al. 2007) conducted tensile tests of nanocellulose/PLA composite films using dog-bone specimen with an overall length 80 mm. The width at grip end was 15 mm and the width at the narrowest part was 10 mm. The gage length was 10 mm, which was much smaller than the gage length recommended by above ASTM standards. Tensile strength and tensile modulus of the composites were measured.

However, such small gage length probably resulted in unreliable elastic modulus due

to the effects of grip slippage. In order to eliminate the grip slippage effect on determination of elastic modulus, optical measurement method of strains will be introduced in our tests, and it will be discussed in detail later in this thesis.

3.3.2 Methods of evaluating toughness

Toughness, the total energy absorbed per unit volume of a specimen up to failure, was measured by calculating the area under the tensile stress-strain curve. When measuring toughness of a material, the rate of strain, specimen parameters and especially flaws may cause large variations in the results (ASTM 2009). Therefore, fracture toughness is often used instead to evaluate the material property independent of specimen geometry.

Fracture toughness is a property which describes the ability of a material containing a crack to resist fracture, and is one of the most important material properties (ASTM 2007). The most popular approach to assess the fracture toughness is linear elastic fracture mechanics (LEFM)(Wu and Mai 1996). However, LEFM method requires limited yielding to ensure the validity(Saleemi and Nairn 1990; Wu and Mai 1996). In other words, it can be successfully applied for brittle materials and materials with small scale yielding. However, LEFM fails to evaluate proper fracture toughness values for ductile polymers where a substantial part of the work to failure recorded as the area below the stress-strain curve is spent on the permanent plastic deformation of the material around the failure zone (Barany, Caigany et al. 2003).

Currently, there are two approaches widely used to evaluate fracture toughness of ductile materials: J-integral method and the essential work of fracture (EWF) theory (Barany, Caigany et al. 2003).

The theoretical analysis of J-integral has been well established and the experimental procedure has been standardized. However, J-integral needs to be obtained under plane-strain condition, which makes application of the J-integral method in the toughness characterization of polymeric thin films impossible (Wu and Mai 1996).

As an alternative to the *J*-integral analysis, essential work of fracture (EWF) method has been successfully used to determine the fracture toughness of many ductile materials (Wu and Mai 1996).

3.2.3.1 Essential work of fracture (EWF)

EWF has been recognized as a material constant, independent of sample geometry. It represents the energy consumed within the fracture process zone where new surface is created (Wu and Mai 1996; Kwon and Jar 2007). In traditional approach, the EWF value is determined using double-edge-notched tensile (DENT) test, for which the specimen is shown in Figure 7. The purpose of notching is to localize the plastic deformation zone. Under the plane-stress condition, total work consumed in a DENT test is composed of two parts: one part is the energy for new fracture surface

creation, i.e., EWF, and the other one is the energy for plastic deformation around the ligament section. Therefore, the goal of DENT tests is to extract the energy for the first part (EWF) from the total fracture energy (Kwon and Jar 2007).

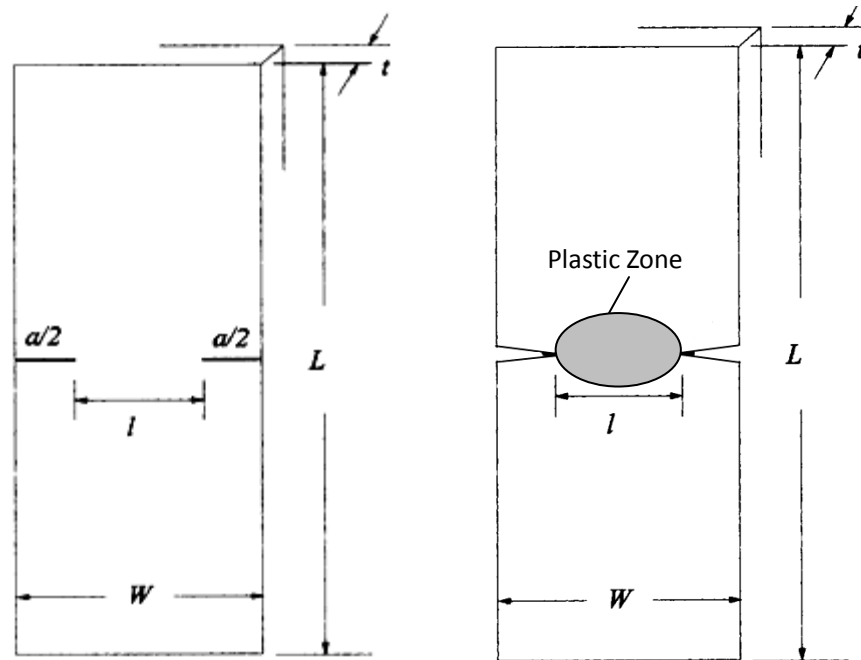


Figure 7. Specimen geometry for double-edge notched tensile (DENT) specimens. The specimen width is W , thickness is t and ligament length is l . (a) specimen before tension; (b) specimen under tension.

To obtain plane-stress conditions and to ensure necking fully developed in the fracture process zone, specimen dimensions are empirically recommended to be (Liu and Nairn 1998):

$$(3 \text{ to } 5)t \leq l \leq \min\left(\frac{W}{3} \text{ or } 2r_p\right) \quad (1)$$

where

t - is the thickness of the specimen, [m]

W - is the width of the specimen, [m]

l - is the ligament length, [m]

r_p - is the radius of the plastic zone at the crack tip, [m]

As described above, the total work to failure of a DENT specimen consists of two terms:

$$W_T = W_e + W_p \quad (2)$$

where:

W_T - is total work to failure, [J]

W_e - is total energy consumed for new fracture surface formation, [J]

W_p - is total energy consumed for plastic deformation, [J]

It is assumed that W_e is proportional to the ligament area and W_p is proportional to the volume of plastic deformation zone (Saleemi and Nairn 1990). The total work to failure becomes

$$W_T = w_e l t + (\beta l^2) w_p t \quad (3)$$

Where:

w_e - is the specific essential work of fracture, [J/m²]

w_p - is the specific work of plastic deformation [J/m³]

β - is shape parameter for the plastic deformation zone (it is assumed that the stress and plastic deformation is uniform across the zone)

When plane-stress conditions apply for all ligament lengths, it is further assumed that

w_e is constant (Saleemi and Nairn 1990). Taking the geometry of the specimen into account, we can get specific work to failure w_t , i.e., W_T/lt , becomes

$$\frac{W_T}{lt} = w_t = w_e + \beta w_p l \quad (4)$$

If w_t is plotted against ligament length l according to equation (4), there should be a linear relationship between w_t and l . The intercept of the best linear fit at zero ligament length is determined as w_e and the slope of the line is βw_p . See typical experimental results in Figure 8.

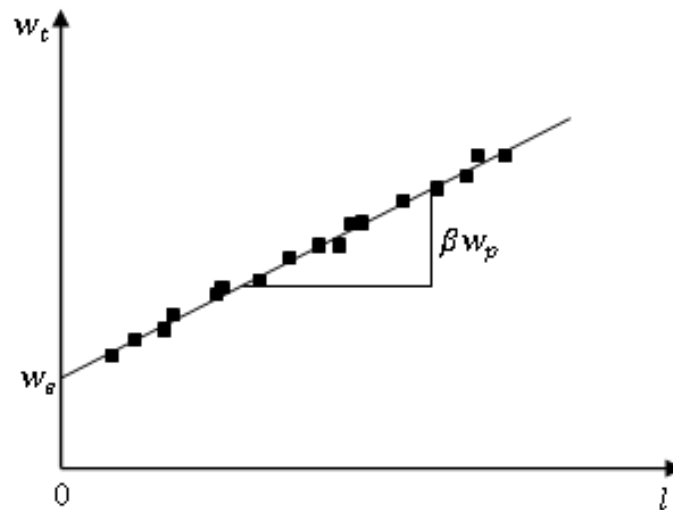


Figure 8. Schematic drawing of the relationship between specific total work to failure w_t and ligament length l . Black dots are typical experimental data points (Liu and Nairn 1998).

Although the traditional experimental method of measuring EWF described above has been well established, there are several major drawbacks of the method:

1. Large amount of samples are needed to evaluate EWF from w_t vs. l characteristics.

2. The method requires that the shape of the plastic deformation zone (β factor) is known or can be estimated.
3. The method assumes uniform level of plastic deformation within this zone.

As explained in the introduction, the prototype formulations were generated in small amounts of thin transparent films. Large amount of specimens is not feasible in this situation.

Therefore, it is necessary to establish a new method that allows us to measure multiple mechanical properties, including tensile strength, elastic modulus, Poisson's ratio, toughness and essential work of fracture, through limited tests. The major challenges are: 1) strains of thin film samples cannot be easily measured by conventional methods (strain gauge or extensometer), which interfere with the measurement due to their stiffness (strain gauge) or weight (extensometers); 2) if an optical measurement of strains method were employed, transparency of the film samples would obstruct track of specimen deformation. Solutions of these challenges and development of this new methodology will be discussed in section 4.2 and 4.3.

4 MATERIALS AND METHODS

Materials and methods for investigating morphology of MFC are described in section 4.1. In order to determine the mechanical properties of prototype MFC-PLA composites, which were in the form of transparent thin films with limited size, development of optical measurement of strains based on digital image correlation (DIC) principle is then discussed. In addition, development of an alternative method of evaluating essential work of fracture (EWF) is also discussed in section 4.3, aiming to evaluate the critical mechanical properties through a small number of tests. These properties include tensile strength, elastic modulus, toughness (specific work to failure), Poisson's ratio and EWF.

4.1 Morphological Characterization of MFC

4.1.1 Materials

Microfibrillated cellulose (MFC) used in this study were from two sources: one batch was obtained by courtesy of Prof. Mike Bilodeau, University of Maine (referred hereafter as MFC type A), and the other batch was purchased from Innventia AB company, Sweden (hereafter referred to as MFC type B). Both types of MFC are in the form of ~5 % water suspension by weight.

4.1.2 Methods

In order to preserve the original composition and structure of MFC, water in the MFC suspension was removed by freeze-drying method. The MFC sample after freeze-

drying process is called MFC aerogel. It was then investigated under SEM microscope.

4.1.2.1 MFC Aerogel Sample Preparation

About 10 ml MFC water suspension of each type was collected in a bottle and then was placed in a freezer overnight. The frozen MFC suspension was then put into a freeze dryer, which allows the frozen water in the sample to sublime directly from the solid phase to the gas phase by reducing the surrounding pressure. The purpose of freeze-drying is to remove water from dispersed MFC, remaining the original composition and structure of MFC. The freeze-dried MFC was kept in a sealed bottle to prevent the reabsorption of moisture. Figure 9 shows MFC suspension before and after freeze drying.

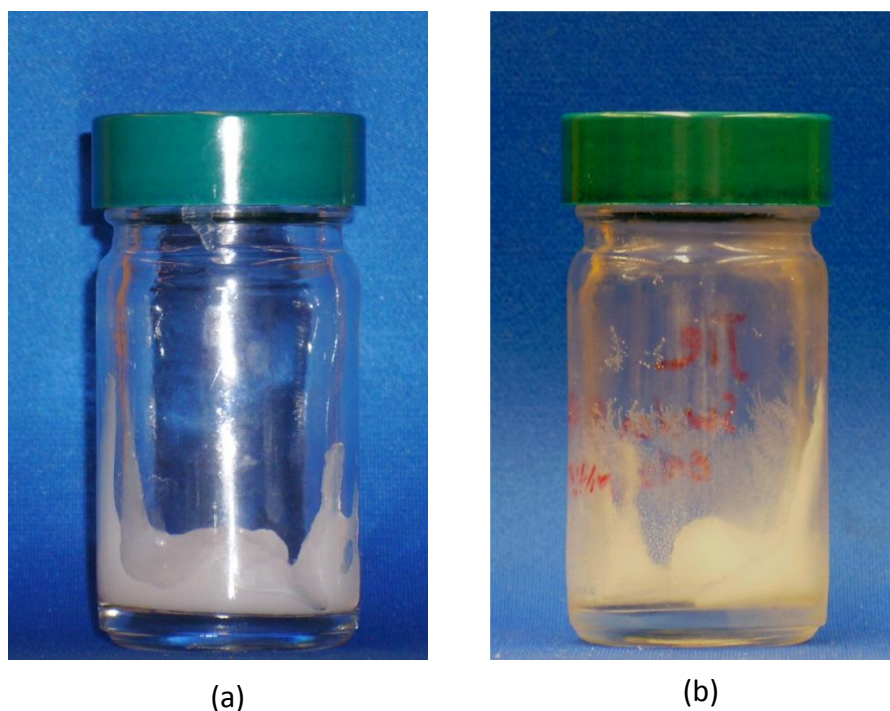


Figure 9. (a) original MFC suspension; (b) freeze-dried MFC aerogel after freeze drying

4.1.2.2 Equipment

Freeze-dried MFC aerogel samples were examined in a FEI Quanta 3D Dual Beam Field Emission Scanning Electron Microscopy (FESEM) at Department of Material Science, Oregon State University. The resolution of this FESEM can be up to 1 nm in scanning transmission electron detector (STED) mode at 30 KV accelerating voltage.

4.1.1.3 Procedure of FESEM Examination

In order to avoid destroying original structure of freeze-dried MFC aerogel, thin MFC aerogel fragments (about 0.5 mm thick) were selected to investigate under FESEM. Since MFC is a nonconductive material, the samples were coated with gold particles of about 3 nm in diameter prior to examination under FESEM. The accelerating voltage applied was 15 kV.

When imaging the microstructure, starting with overall view of the sample, three random locations on the MFC aerogel sample were selected as areas of interest to investigate the morphology of the features visible in the original view under higher magnification. Then the magnification on each of area of interest was gradually increased to inspect various levels of material organization in the sample. The transition to the next level of magnification was performed in the same manner. The procedure was repeated within each of the areas of interest until the higher magnification did not reveal any finer level of material organization or highest resolution available with the instrument was reached.

4.1.3 Expected Output

For each type of freeze-dried MFC aerogel (type A and B), SEM micrographs at different levels of magnification need to be obtained for morphological characterization of MFC and their network structure.

4.2 Mechanical Characterization of Bulk MFC-PLA Nanocomposites

Critical mechanical properties including tensile strength, elastic modulus, toughness of bulk MFC-PLA nanocomposite films are the properties of interest when evaluating the prototype composite formulations. However, accurate measurement of strains on thin film samples is a challenge. The film specimens are too thin for the conventional methods: the thickness and stiffness of strain gauges is comparable or greater than that of the measured film specimen, while the weight of extensometers easily distorts the specimens in the lateral direction. Although the change in position of the cross head of the testing machine is often accepted as a measure of the specimen elongation, it requires large gage length (250 mm as indicated in ASTM standards) in order to minimize the effects of grip slippage on test results. While the feasible gage lengths for our samples were less than 40 mm, there is no way to guarantee the elongation measured by the movement of the grip is reliable.

In order to overcome above challenges, an optical measurement method based on digital image correlation (DIC) principle was introduced to measure the deformation and strains of the tensile film samples. This method will be discussed in detail in section 4.2.2.

4.2.1 Materials

All the PLA control film samples and MFC-PLA nanocomposites samples were cast by Melissa Taylor, a graduate student at the Department of Wood Science and

Engineering, Oregon State University. The procedures are described in section 4.2.1.2 and section 4.2.1.3.

4.2.1.1 Microfibrillated Cellulose (MFC)

MFC used for casting MFC-PLA nanocomposites was described in section 4.1.1.

4.2.1.2 Polylactic acid (PLA) 3051D (NatureWorks®)

To prepare PLA control film, PLA 3051D pellets were dissolved overnight in dichloroethane with stirring. Control film was cast from dichloroethane (5.3 wt% solution, 5.9 g solution) over Si wafers in a 8 cm diameter mold, evaporated in a desiccator overnight, then dried at 40 °C for several hours under vacuum.

4.2.1.3 MFC-PLA nanocomposite films

MFC without lactide treatment and lactide treated MFC were used to reinforce PLA.

4.2.1.3.1 MFC without lactide treatment in PLA

MFC pretreatment: MFC was sonicated with 10% NaOH 6 hours, washed with diH₂O till neutral, then solvent exchanged into methanol, then into dichloroethane to a final concentration of 1mg/mL.

0.25% MFC in PLA: MFC treated as above was added to 5.6 g a 5.3 wt% PLA 3051D

solution (taken from control solution) to get a 0.25 wt% MFC to PLA loading. Then entire volume of solution was cast over Si wafers in a 8 cm diameter mold, evaporated in a desiccator overnight, and dried at 40 °C for several hours under vacuum.

0.1% MFC in PLA: Samples were prepared as described above, with MFC added to 5.6 g of the 5.3 wt% PLA 3051D control solution to a 0.1% MFC to PLA loading.

4.2.1.3.2 Lactide treated MFC in PLA

MFC Pretreatment: MFC sonicated 6 hours in 10% NaOH, washed till neutrality, was solvent exchanged into N-methyl pyrrolidone (NMP), then reacted with lactide to a 10 fold molar excess to MFC surface hydroxyls. Stannous octoate and co-catalyst triphenylphosphine were both added at 1:2500 molar ratio to lactide, and reaction was allowed to reflux at 180 °C for one hour. MFC was washed with NMP, then solvent exchanged into dichloroethane.

0.25% Lactide treated MFC in PLA: Lactide treated MFC in dichloroethane was loaded into 5.4 g 5.3 wt% PLA 3051D solution (same solution as for control film) at 0.25% MFC to PLA and cast over Si wafers in 8 cm mold, evaporated in a desiccator overnight, then dried at 40 °C for several hours under vacuum.

0.1% Lactide treated MFC in PLA: Samples were prepared as described above, with

MFC added to 5.6 g of the 5.3 wt% PLA 3051D control solution to a 0.1% MFC to PLA loading.

Two different types of MFC were used in our experiments: MFC from University of Maine (type A) and MFC from Innventia AB company, Sweden (type B).

Table 7 and Table 8 summarize the numbers of specimens for mechanical testing in this project. Percent MFC loaded listed in the tables were based on weight percent. Opposite to lactide treated MFC, MFC without lactide treatment were called untreated MFC.

Table 7. Numbers of specimens with type A MFC

MFC treatment		Percent MFC Loaded			
		0%	0.10%	0.25%	0.50%
Control: Pure PLA Films I		3			
MFC-PLA Films	w/Untreated MFC		6	6	3
	w/ Lactide Treated MFC		5	6	2

Note: MFC loading levels were based on weight percent.

Table 8. Numbers of specimens with type B MFC

MFC treatment		Percent MFC Loaded			
		0%	5%	10%	15%
Control: Pure PLA Films II		14			
MFC-PLA Films	w/Untreated MFC		4	5	5
	w/ Lactide Treated MFC		5	6	6

Note: MFC loading levels were based on weight percent.

4.2.2 Methods

Mechanical properties of MFC-PLA nanocomposite films were determined by tensile tests with testing speed of 1.5 mm/min, which results in the initial strain rate of 0.05.

ASTM D882-09 recommends that initial strain rate should be 0.1 when percent elongation at break of a sample is less than 20%. Since the percent elongation at break of our brittle PLA and MFC-PLA composite films was less 5%, initial strain rate of 0.05 was then selected.

Tensile strength could be easily obtained by dividing the maximum load acquired from the output of the Instron testing machine by the original minimum cross-sectional area of the specimen. However, in order to measure reliable elastic modulus and toughness, a method of measuring reliable strains had to be developed.

4.2.2.1 Development of methodology of optical measurement of strains using DIC

Digital Image Correlation (DIC) is an optical method to measure deformation on an object surface. The method tracks the gray value pattern in small neighborhoods called subsets or subareas during deformation. The size of subsets controls the area of the image that is used to track the displacement between images. The other important parameter of the DIC analysis is step size (d_{ss}), which is the distance between two centers of neighboring subsets. It controls the spacing of the points that are analyzed during correlation. For 3D measurement, two cameras are used to observe an object from two slightly different directions (or angles). The position of each point on the object is then focused on a specific pixel in the camera plane. Knowing the imaging parameter for each camera and the orientation of the cameras with respect to each, the position of each object point in three dimensions can be

calculated. As the object deforms, the resulting deformations and strains can be calculated by comparing the position of each object point to reference position by applying a correlation algorithm. This method has been successfully applied in mechanical tests of many materials and structures of various sizes from sub-millimeter to meters (Muszyński and Launey 2010). Figure 10 shows the setup of tensile testing on MFC-PLA film samples employing optical measurement of deformation based on DIC principle.

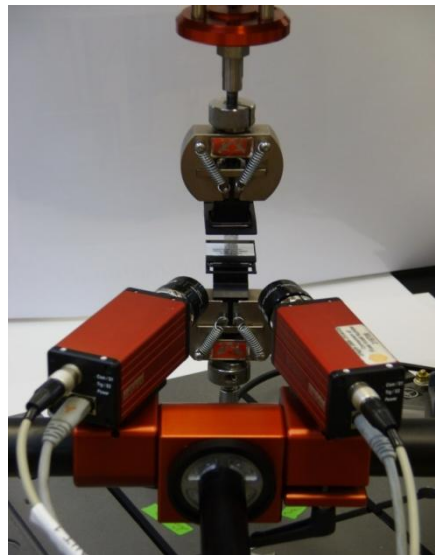


Figure 10. Setup of tensile testing on transparent films employing optical measurement of deformation based on DIC principle.

4.2.2.1.1 Problem statement and solutions

The principle of DIC is easy to understand, but it is not easy to apply when the object is a transparent film sample. The biggest issue is that it is hard to optically separate a transparent specimen from its background. The solution presented below is a result of a long trial and error process, description of which is beyond the scope of this thesis.

First, a random speckle pattern was applied on the transparent film specimens so that the cameras can record and track the movements of speckles and then take these movements as the deformation of the specimen.

Second, a smooth white background was set behind the specimen so that the objects in the background did not interfere with the measurement.

Third, a diffused light was projected on the testing scene to reduce the shadows of speckles on the white background.

4.2.2.1.2 Accuracy and precision assessment

According to ASTM E2655 (ASTM 2008), accuracy is the degree of closeness of a measured or calculated quantity to its actual value. Precision, also called reproducibility or repeatability, is the degree to which further measurements or

calculations show the same or similar results. The accuracy and precision of the optical measurement techniques based on DIC cannot be provided by the manufacturers in absolute numbers because the measurements may be conducted on images of very different scales and the uncertainty is affected by many external factors (quality of the optics, lighting, position of the cameras, operator skills etc.). Therefore, the accuracy and precision for the optical measurements have to be evaluated individually for the specific experimental setup and re-evaluated when any changes in the setup is made.

Accuracy and precision of the method were assessed on three levels:

1. For each individual specimen: the accuracy and precision was evaluated using 6 images for undeformed specimen, when both displacements and strains were expected to be zero.

Figure 11 shows an example of the accuracy and precision evaluation for an individual specimen (specimen ID: P20). Symbols u and v represent horizontal displacements and vertical (same direction as applied load) displacements respectively. Symbols ϵ_{xx} and ϵ_{yy} represent horizontal strain and vertical strain respectively. The heights of error bars (standard deviations) represent the precision.

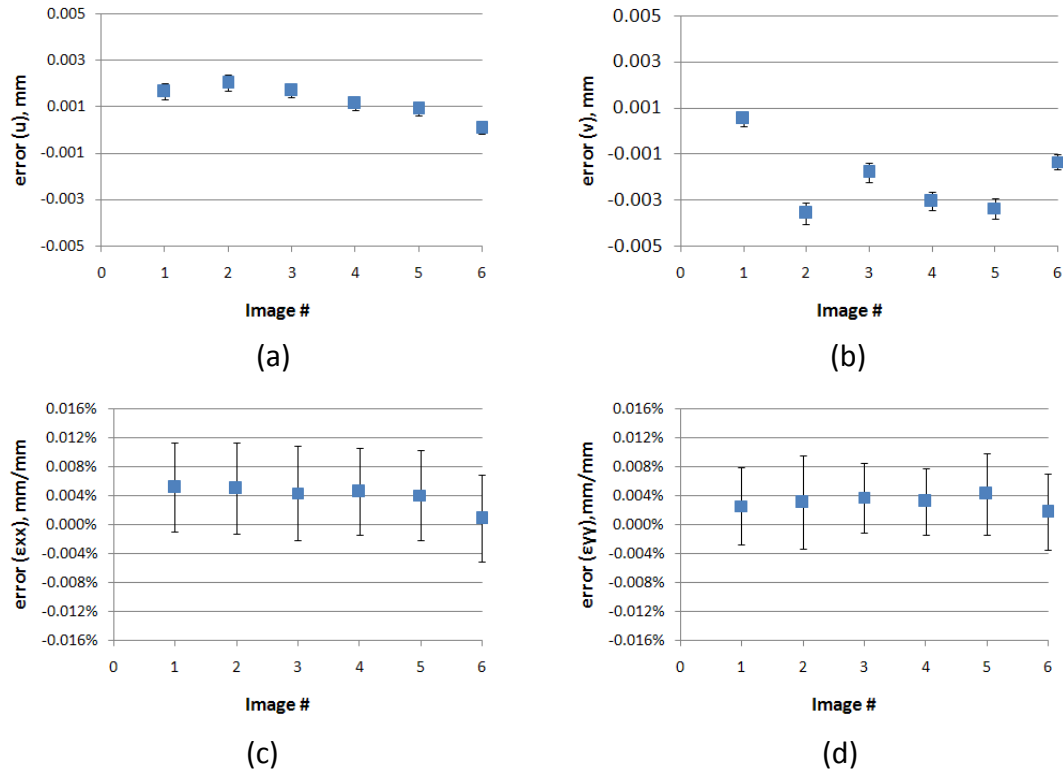
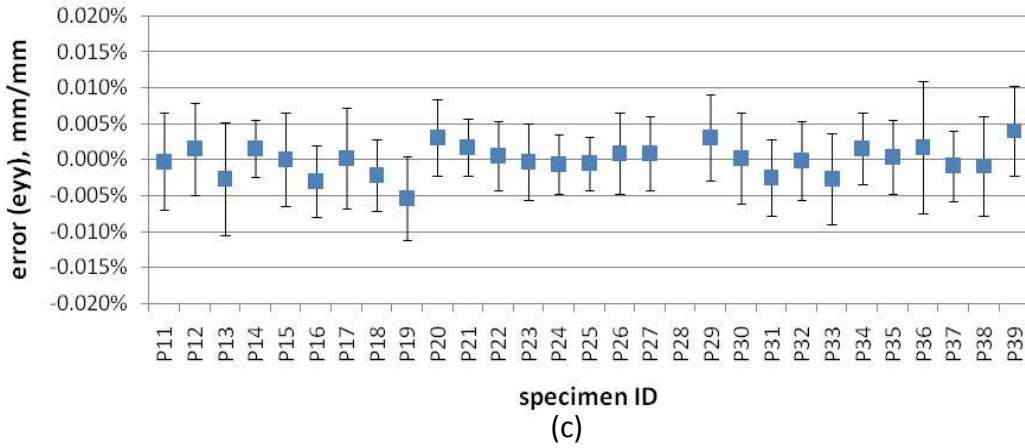
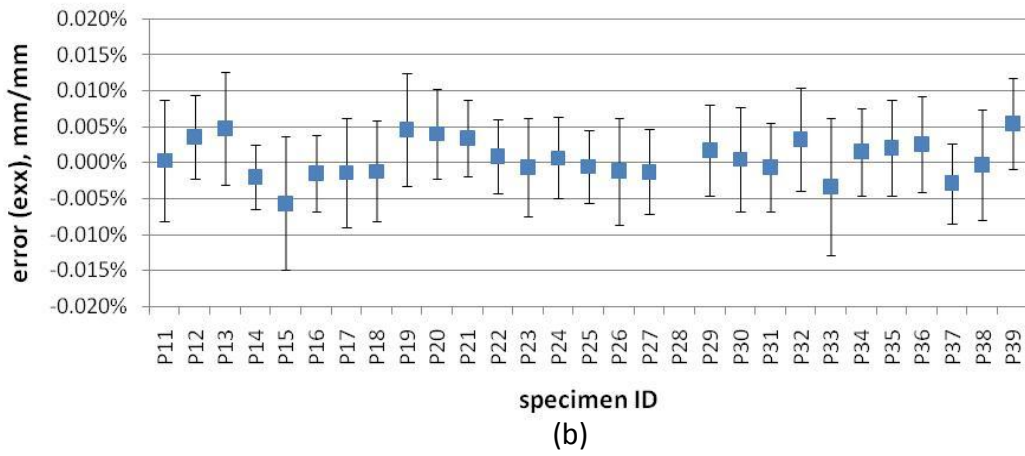
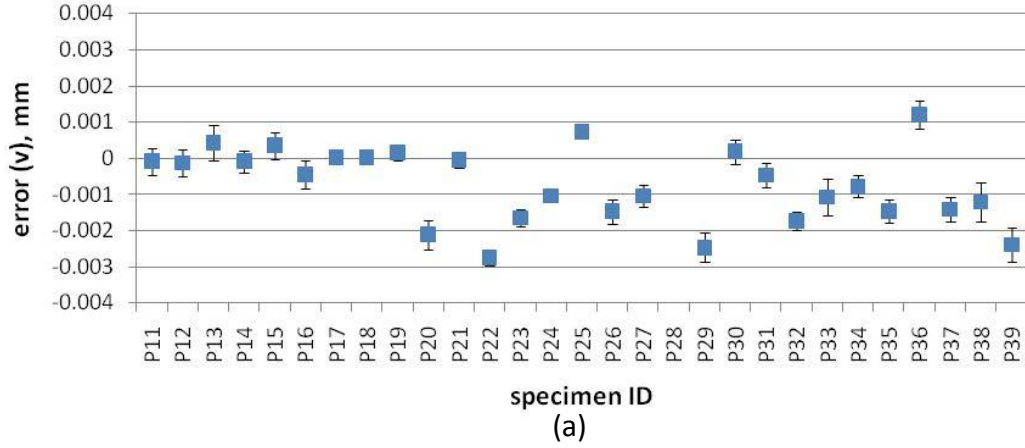


Figure 11. Accuracy and precision assessment for an individual specimen: (a) horizontal displacement error (u); (b) vertical displacement error (v); (c) horizontal strain error (ϵ_{xx}); (d) vertical strain error (ϵ_{yy})

2. Average accuracy and precision for each specimen were calculated based on the 6 individual measurements taken in step 1.

Figure 12 shows accuracy and precision evaluation for each specimen in the preliminary test series. Every data point is the average of six corresponding values evaluated in level 1.



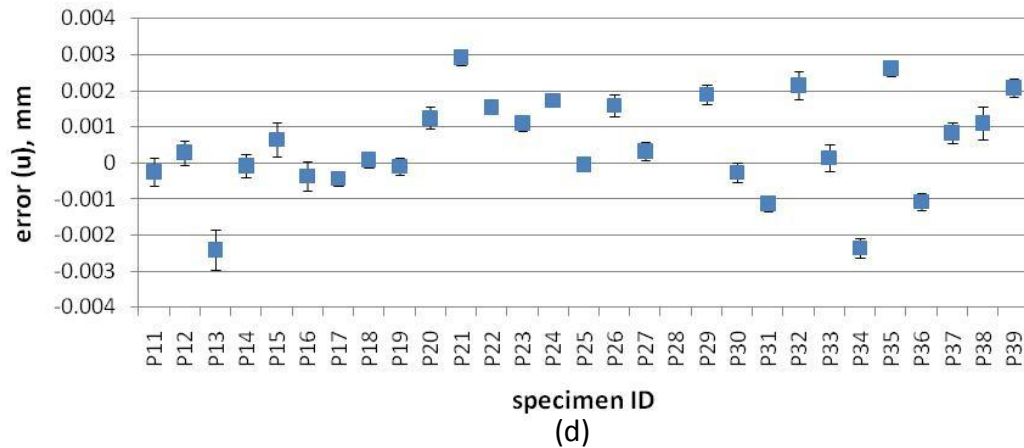


Figure 12. Accuracy and precision assessment for each specimen: (a) horizontal displacement error (u); (b) vertical displacement error (v); (c) horizontal strain error (ϵ_{xx}); (d) vertical strain error (ϵ_{yy})

- Overall Accuracy and Precision Assessment—evaluated as the average accuracy and precision for all specimens used throughout the test series.

Figure 13 shows the box plots of the overall accuracy and precision assessment for throughout the test series. Displacement and strain errors reflect the overall accuracy of displacement and strain respectively. Standard deviations of displacement and strain represent the overall precision of displacement and strain respectively.

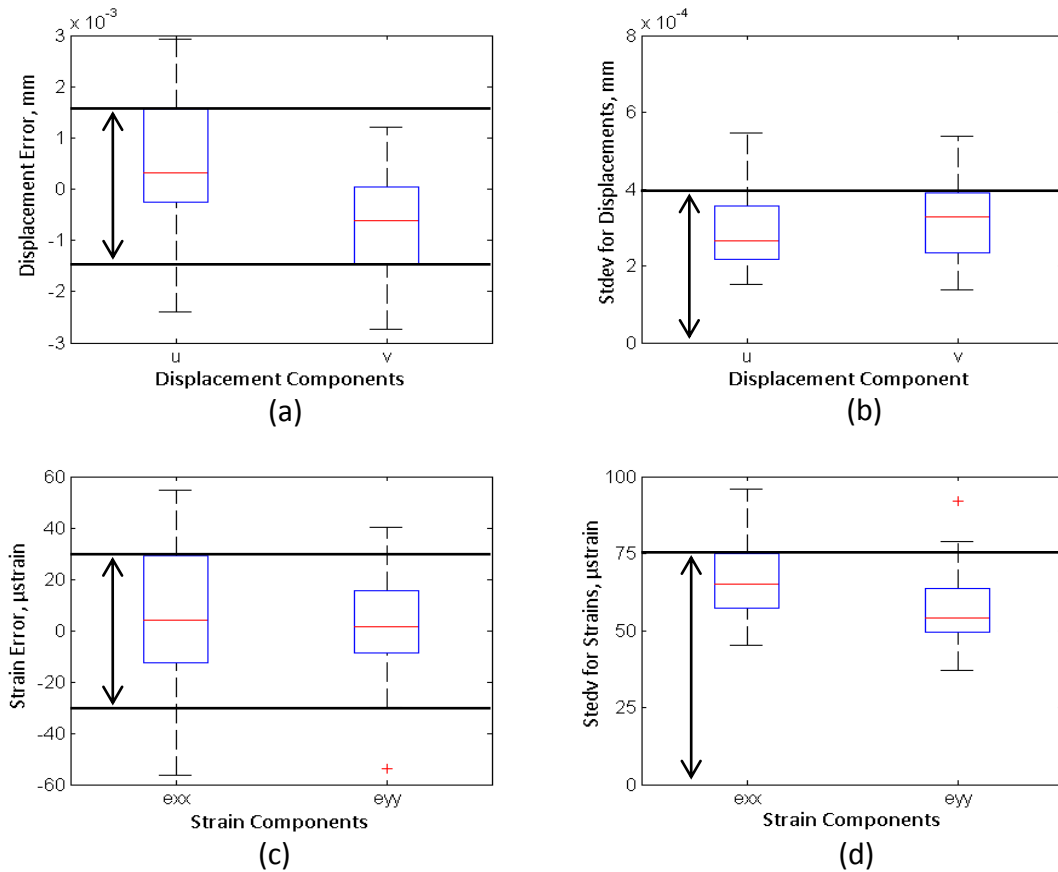


Figure 13. overall accuracy and precision assessment: (a) accuracy of displacement; (b) precision of displacements; (c) accuracy of strain; (d) precision of strains

Figure 13 (a) and (c) indicate that, for throughout the test series, the accuracies of displacements and strains in both horizontal and vertical directions were $\pm 1.5 \mu\text{m}$ and $\pm 30 \mu\text{strain}$, respectively. Figure 13 (b) and (d) show that the precisions of displacements and strains in both horizontal and vertical directions were $0.4 \mu\text{m}$ and $75 \mu\text{strain}$, respectively.

The high accuracies and precisions of displacements and strains indicated that optical

measurement method based on DIC principle had been proven a robust method of measuring deformations and strains for transparent thin film samples.

4.2.2.1.3 Study on the accuracy and precision of optical measurement while using various speckle patterns on clear thin films

In order to study influence of speckle patterns on accuracy and precision of optical measurement of strains of transparent thin films, eight speckle patterns printed with a laser printer (HP Laser Jet 9050dn) (see Figure 14) and two speckle patterns spray-painted with KRYLON black paint were evaluated for accuracy and precision assessment. A random pattern provides a random array of gray scale values, and each subset in an image should be unique. Printed pattern 07 was the build-in granite texture in MS word. Printed pattern 07 was obtained from web. It was generated by a Java code (Gallery 2011). Note that if the speckle size generated is too small, for instance less than two pixels, its actual location and light intensity will have higher uncertainty than that for a speckle of larger size. However, if speckle size is too large, the accuracy of measuring small strains will be limited (Hung and Voloshin 2003). One 50mm X 15mm with narrowest part of 10 mm dog-bone specimen was cut for each pattern. Five images of un-deformed specimen were evaluated for each speckle pattern.

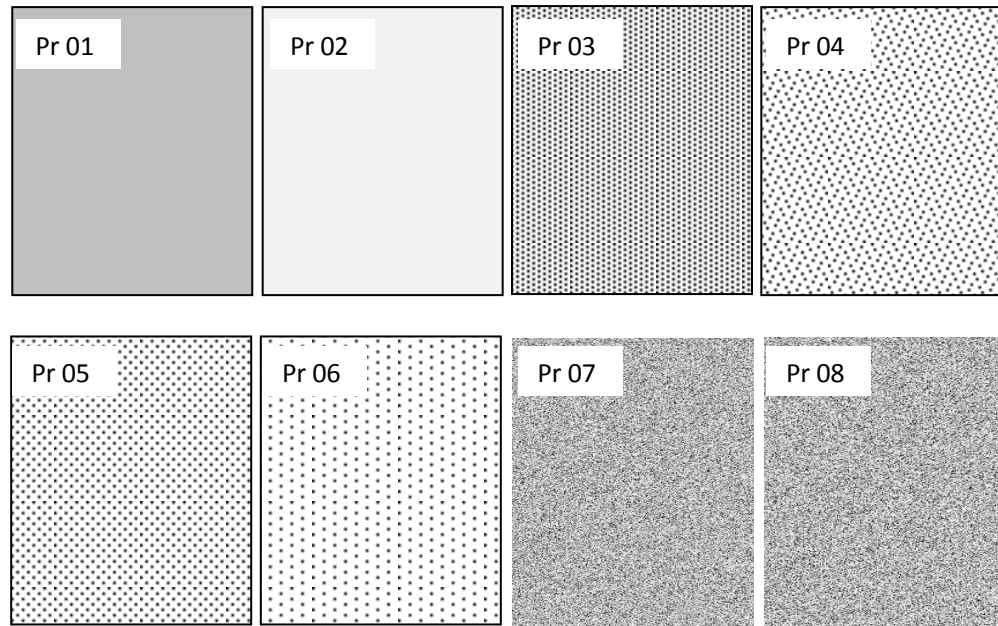


Figure 14 Eight different printed speckle patterns: Pr01 and Pr02 with uniform gray scale but different gray scale levels; Pr03-Pr06 with regular speckle patterns but different spacing; Pr07 (Gallery 2011) and Pr08 with random speckle patterns

Same as accuracy and precision assessment on level two described in section 4.2.2.1.2, average accuracy and precision of strains in vertical direction (ϵ_{yy}) and horizontal direction (ϵ_{xx}) for each specimen were calculated and compared. The results are shown in Figure 15 to Figure 18 The label "Pr" stands for printed patterns, and "Pa" stands for painted patterns. For convenience of comparison, all the errors were converted to absolute values, and they represent accuracies. The heights of error bars represent precisions.

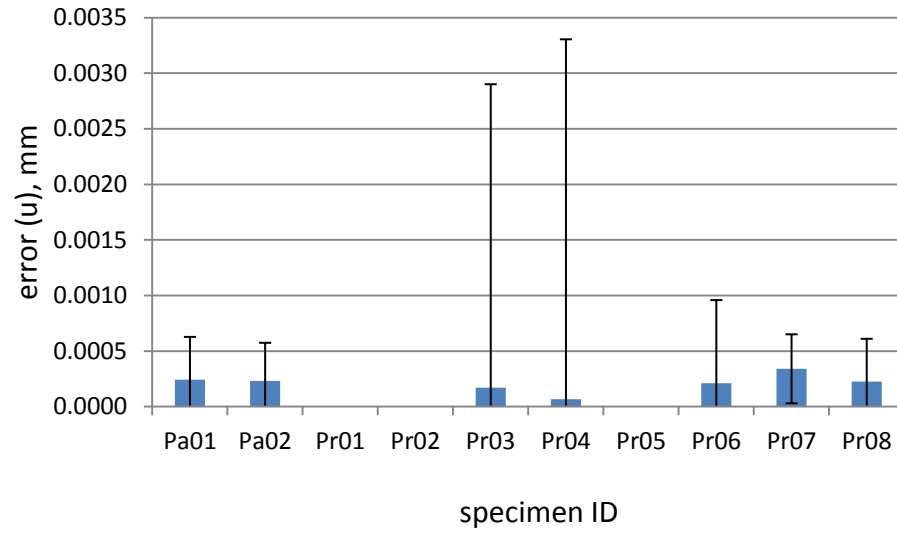


Figure 15. Accuracy and precision of displacement in horizontal direction for all patterns

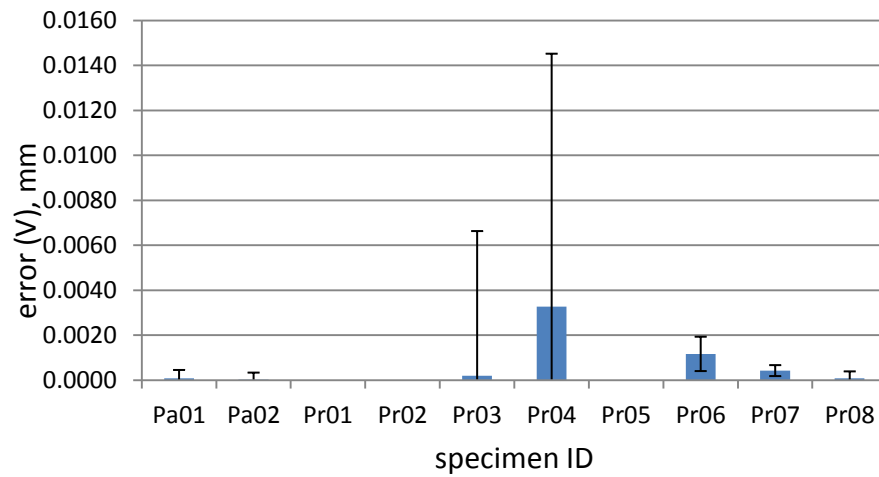


Figure 16. Accuracy and precision of displacement in vertical direction for all patterns

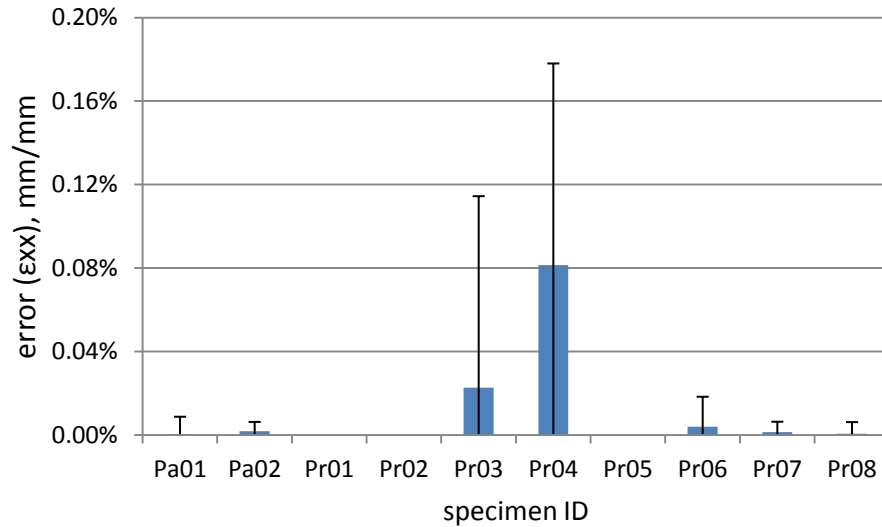


Figure 17. Accuracy and precision of strain in horizontal direction for all patterns

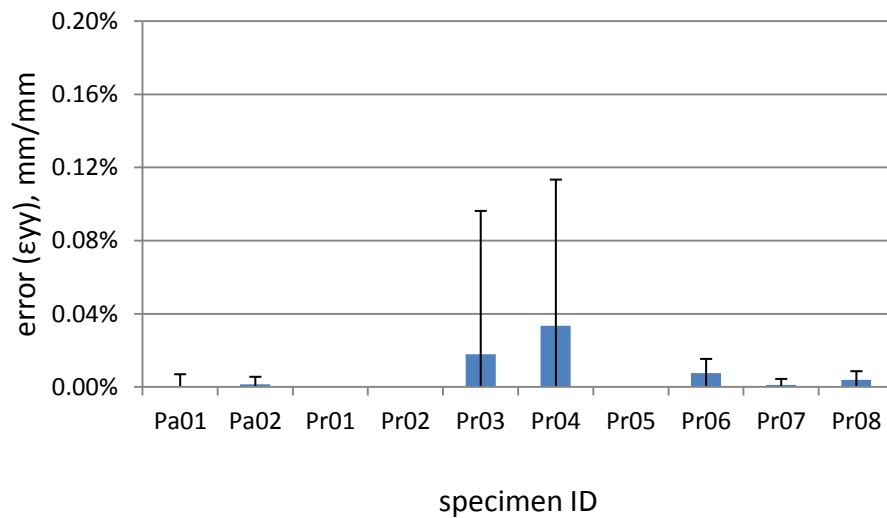


Figure 18. Accuracy and precision of strain in vertical direction for all patterns

Printed patterns Pr01, Pr02 and Pr05 could not be analyzed. Since the DIC method relies on the existence of a distinct gray scale pattern in a region composed of a subset of pixels (Lu and Cary 2000), uniform gray scale patterns couldn't be used for digital image correlation. Printed pattern 05 had the same speckle spacing in both

vertical and horizontal directions, which provided the same gray scale values in both directions. Such pattern would also impede the correlation computation.

Although other patterns (Pr03, Pr04 and Pr06) of printed regular speckles with different spacing in vertical and horizontal directions could be analyzed, they had poor precisions (large error bars compared patterns Pa01, Pa02, Pr07 and Pr08) of displacement and strain measurement. Patterns Pr03 and Pr04 had extremely large error in vertical and horizontal strains, which indicated bad accuracy of strain measurements.

However, printed random patterns Pr07 and Pr08, and painted random patterns Pa01 and Pa02 provided very good accuracy and precision of displacement and strain measurements. The accuracies of displacements and strains in both directions were less than $\pm 1 \mu\text{m}$ and $\pm 40 \mu\text{strain}$ respectively. The precisions of displacements and strains in both directions were less than $0.4 \mu\text{m}$ and $80 \mu\text{strain}$, respectively.

Therefore, it is essential to the DIC method that an object surface has to be applied with a random speckle pattern to obtain good accuracies and precisions for measurements of displacements and strains of the object. In the study for measurement of essential work of fracture of transparencies, specimens were applied with random speckle pattern Pr07.

4.2.2.2 Sample Preparation for tensile testing

1. Three dog-bone specimens were cut out of a neat PLA or MFC-PLA nanocomposites film sample using a razor blade. The specimens had an overall length of 50 mm, a width at the grip end was 15 mm, and the width at the narrowest part was 10 mm.
2. Width and thickness of the narrow part of each dog-bone specimen were measured using a caliper (± 0.01 mm) and a micrometer (± 0.001 mm) respectively.
3. To obtain random speckle pattern on the surface of the specimens, all the specimens were covered with a random speckle pattern applied with KRYLON black spray paint. At least 60% surface of the specimens need to be covered with black speckles following the density of pattern Pa01. Specimens before and after applying random speckles are showed in Figure 19.

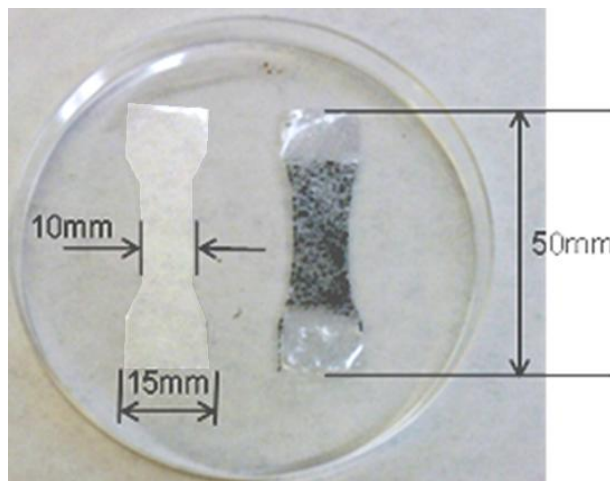


Figure 19. Specimens for tensile testing before and after applying random speckles

4.2.2.3 Equipment

The experimental setup is mainly composed of two parts: an universal testing machine setup for tensile testing and optical measurement unit.

Tensile testing was conducted on an Instron mechanical testing machine, from which loads and positions of the grip could be acquired. Instron ElectroPuls E1000 with load capacity ± 1000 N was used in our testing. The resolutions of the load cell and position measurement were less than 0.01 N and 0.001 mm, respectively.

Optical measurement was based on the DIC principle described in section 4.2.2.1. Images of samples during the tensile testing were acquired by a pair of lenses and cameras. Schneider Kreuznach (XENOPLAN 1.4/23-0512) lenses and AVT Dolphin F-201B cameras with resolution of 1628 x 1236 were used for image capture. Program for strain computation was Vic 3D (2007/2009 edition).

4.2.2.4 Procedures for mechanical tests of bulk MFC-PLA nanocomposites

There were four major steps for mechanical tests of bulk MFC-PLA nanocomposites films:

1. Set up and calibration of the universal testing machine and the optical measurement system. The detailed procedures are described in Appendix A.
2. Assessment of accuracy and precision on an un-deformed specimen.
3. Mechanical testing and image acquisition.

4. Processing of numerical and image data.

4.2.3 Expected Output and Measured Quantities

The procedures described in the previous sections yielded the following sets of data:

- Measurements of specimen dimensions (width and thickness) were manually tabularized.
- Load and positions of crosshead of Instron for each tensile test were recorded at the rate of 10 measurements per second with the data acquisition unit integrated with the testing machine and saved in comma-separated-values (.csv) text files available for further processing. Maximum tensile load (P_{mx}) was automatically recorded by the system.
- The optical measurement (DIC) system collected the time-stamped images of the deformed specimens recorded simultaneously by the two cameras at the rate of 1 frame per second (fps). The corresponding loads and displacements measured with the Instron testing machine were probed at the same rate using an analog data acquisition system integrated with the DIC unit. The time stamps and recorded analog data have been saved in comma-separated-values (.csv) text files available for further processing.

4.2.4 Data Treatment

4.2.4.1 Tensile strength

Tensile strength was calculated by following equation:

$$\sigma_{UTS} = \frac{P_{max}}{A} \quad (5)$$

Where:

σ_{UTS} : Ultimate tensile stress, or tensile strength, [MPa]

P_{max} : Maximum load, [N]

A: Original cross-sectional area of the narrow part of the sample, [mm²]

4.2.4.2 Stress-strain curves

Elastic modulus is determined by the slope of the linear portion in stress-strain curve. The nominal stress was calculated by dividing the load by original cross-sectional area of the narrow part of the sample.

By using Vic3D software, horizontal and vertical displacements (output as U and V respectively) as well as horizontal and vertical strains (output as ϵ_{xx} and ϵ_{yy}) at every single point or subset in the area of interest (AOI) on the specimen surface can be calculated. Furthermore, strains within the AOI can be mapped.

Since the strain maps of the area of interest on the specimen surface calculated with the DIC software are inhomogeneous (Figure 20) a number of strategies may be used to calculate the representative strain in the specimen. In this study, the representative strain in the specimen was calculated by four methods. Comparison of the outcomes will be discussed in section 5.2.2.

The first three methods (referred hereafter as methods a, b and c respectively) were based on the strain maps for the AOI obtained from the DIC software.

a) The representative specimen strain for each loading stage was calculated as the average vertical strain component value ϵ_{yy} for the entire area of interest (AOI) (Figure 20a)

b) The representative specimen strain for each loading stage was calculated as the average vertical strain component value ϵ_{yy} for the selected failure zone or plastic deformation zone of a sample. The failure zone has been identified from the vertical strain component map calculated for the last image before the failure as marked with the white box in Figure 20b.

c) Strain was calculated by using “virtual extensometer”

On the 2D plot of the vertical strain component map, two narrow rectangles were selected at top and bottom of the AOI respectively marked as white narrow boxes in Figure 20c. The vertical position of the center of each rectangle could be read and recorded as Y_t and Y_b in mm. Distance between these two centers could be regarded as virtual gage length. Mean displacements of points within each narrow rectangle were automatically calculated with the testing time, and recorded as V_t and V_b in mm. Then strains were expressed as:

$$\epsilon = \frac{\Delta L}{L_0} = \frac{V_t - V_b}{Y_t - Y_b} \quad (6)$$

where:

ΔL - change of relative position of centers of top and bottom rectangles. It can be regarded as elongation of the specimen between top and bottom rectangles.

L_0 - the distance between two centers of top and bottom rectangles. It can be regarded as virtual gage length.

This method simulates measurement with a conventional extensometer, a method used in other published studies, and may be used for comparisons with published data.

- d) In the fourth method (referred hereafter as method d), strain was calculated based on the positions of the Instron crosshead. The movement of Instron crosshead was considered as the elongation of the specimen along longitudinal direction. Strain was then calculated by dividing the elongation by gage length, which was the distance between upper grip and lower grip. As discussed above, this method is charged with a risk of incorporating the slippage in the grips in the measurement of specimen displacement, as well as compliance of the entire load chain.

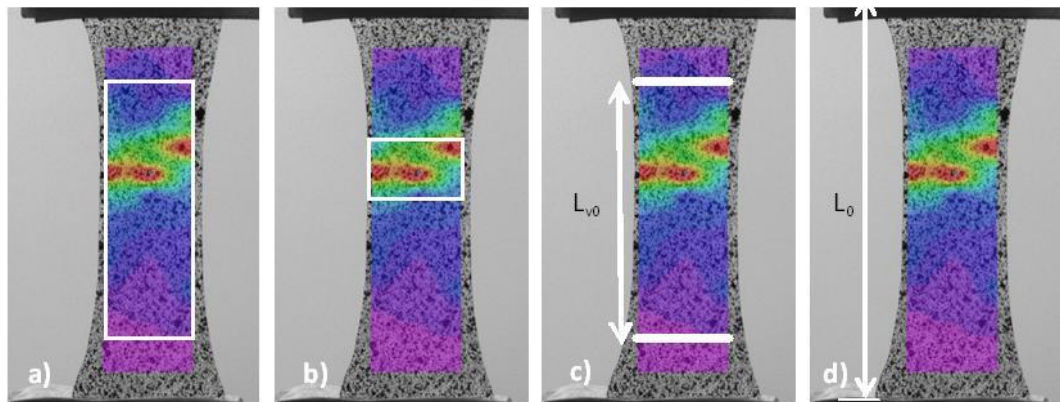


Figure 20. Four methods of strain calculation: a) means strain over the AOI; b) mean strain within plastic deformation zone; c) based on virtual extensometer; d) based on Instron crosshead movement

Combined with stress, typical stress-strain curves obtained using four different methods are shown in Figure 21.

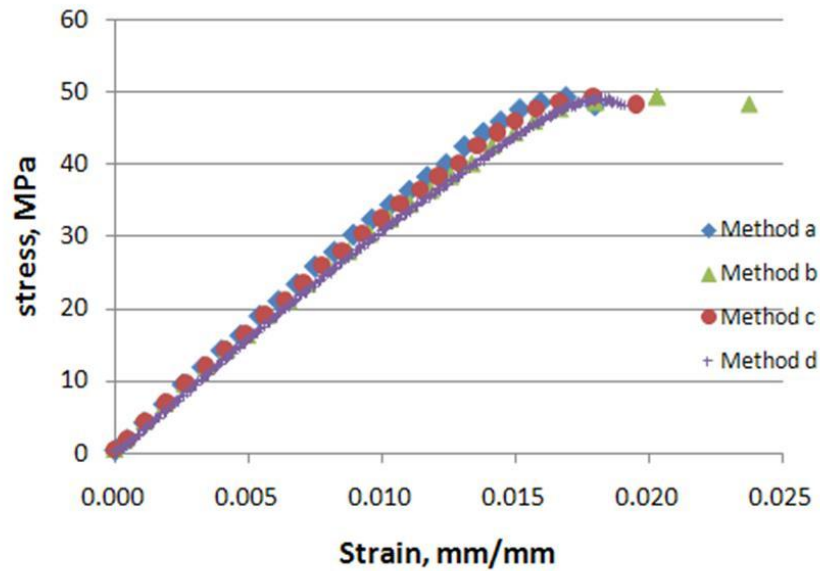


Figure 21. Typical stress-strain curves generated using four different approaches

Stress-strain curves obtained from these four methods match reasonably well while the specimens were loaded within the elastic region. However, method d (based on movement of crosshead) generated slightly lower slope of elastic region. The lower slope of elastic region, which may indicate grip slippage. When the strains are calculated based on the crosshead movement the slippage at the grip is incorporated in the measurement of the deformation of the specimen and consequently the strains are overestimated.

In Method b strains are measured optically in the strain concentration zone where

the fracture eventually occurs. Strains measured in the failure zone alone appear to reach the proportional limit earlier than might be expected from the stress-strain curve generated using other methods. Toughness calculated from this method is less dependent on the specimen geometry and therefore may be somewhat closer to a true material property. It is hoped essential work of fracture (EWF) would be a better way of coping with this problem.

4.2.4.3 Elastic modulus

The elastic modulus (E) of MFC-PLA nanocomposites films reported in this thesis was calculated based on method c (virtual extensometer). It makes the values comparable to other published values.

4.2.4.4 Toughness

Toughness is the total energy absorbed per unit volume of a specimen up to the point of rupture. The toughness of a sample is essentially the same as the area under the stress-strain curve. Once stress and strain were calculated, the area under the stress-strain curve could be calculated numerically. Toughness of MFC-PLA nanocomposites films reported in this thesis was calculated based on method c (virtual extensometer). It is worth pointing out that the value of toughness defined that way will strongly depend on which method of calculation of the representative specimen strains is selected. It can be easily demonstrated that substantially

different values of the work to failure would be obtained from diagrams with strains obtained from method b (mean strain within failure zone), which may be somewhat closer to calculate a "true toughness" of a material. This is because the failure is a localized phenomenon, which is not well reflected when representative strains based on the entire specimen length are used to build stress-strain curves. Clearly, the longer specimen is, the smaller the effect of the plastic deformation in the failure zone occurs, and consequently the smaller calculated area under the stress-strain curve is.

4.2.4.5 Poisson's Ratio

The Poisson's ratio is the ratio of transverse strain to axial strain on a material stressed along one axis (Peng and Zhang 2007). Average horizontal strain (transverse strain) ϵ_{xx} and average vertical strain (axial strain) ϵ_{yy} for the entire area of interest (AOI) at each loading stage could be calculated based on DIC. Poisson's ratio may be found as the slope of linear portion of the curve on a plot of the absolute value of ϵ_{xx} vs. ϵ_{yy} . A typical $abs(\epsilon_{xx})$ vs. ϵ_{yy} curve for MFC-PLA films is shown in Figure 22.

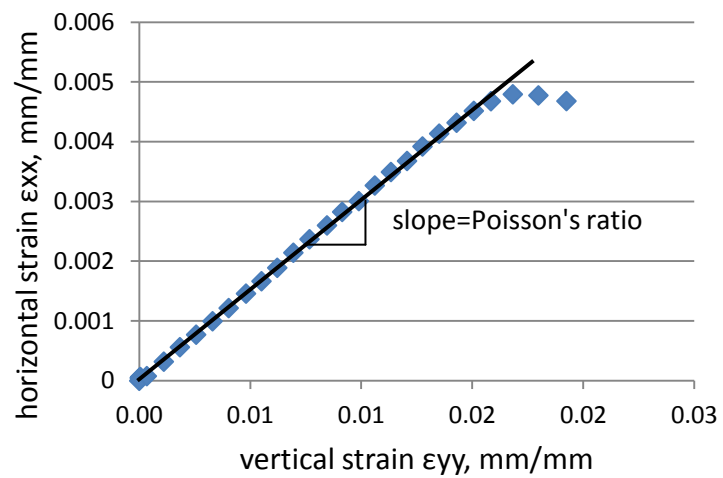


Figure 22. Typical plot of an absolute value of the horizontal strain vs. vertical strain curve for MFC-PLA film samples

4.3 Developing an Alternative Method of Evaluating Essential Work of Fracture (a proof of concept)

As seen from the discussion above, toughness calculated as a specific work to failure is not a true material characteristic, in the sense that its value is strongly dependent on the specimen geometry. Therefore, a different approach is needed.

The optical measurement allows an insight in the strain fields in the specimens beyond the failure. That way the recovered elastic strains and the irrecoverable plastic deformation can be determined from strain maps after the specimen fracture. It is an opportunity for an alternative experimental approach to measure essential work of fracture. However, this approach needs to be proved first. The study aimed at the proof of concept is presented below.

4.3.1 Materials

Printable, ductile and transparent polyester film sheets (PP 2500), purchased from 3M company, were used to substitute for MFC/PLA composite in this study. The film sheets were in the form of 279 mm × 216 mm × 0.1 mm. They were cut into 25 mm × 100mm bars with random black speckle pattern printed on.

Specimens were tested in the DENT configuration shown in section 3.3.2. The notches were cut using a razor blade along a printed line on the film bar, so that they can be well aligned. Specimens with four different ligament lengths were prepared for the experiment, three of which were smaller than 1/3 of width as recommended in

(Saleemi and Nairn 1990) and one with the ligament length larger than 1/3 of width. Each ligament length had 5-6 repetitions. Ligament lengths and numbers of specimens are listed in Table 9.

Table 9. Ligament length and number of specimens tested for measurement of EWF

Ligament length, mm	Number of specimens
3	6
5	5
6	5
7	6
12	6
17	6
24	5

In addition, in order to prove the feasibility of integrating measurement of EWF into determination of other mechanical properties, such as tensile strength, Poisson ratio and elastic modulus, five 25 mm × 100 mm unnotched dog-bone specimens with the narrowest part of 15 mm were cut from the film sheets and used for measuring the EWF using optical measurement. The reason why specimens with total widths of 15 mm were used was that testing duration could be dramatically reduced compared to those with total widths of 25 mm. Since EWF is expected to be independent of specimen geometry, specimens with total widths of 15 should be sufficient.

4.3.2 Methods

All the tensile tests were performed on the 1 KN Instron (ElectroPuls E1000) testing frame described in 4.2.2.3. The testing speed was 0.5 mm/min. The corresponding loads and displacements measured with the Instron testing machine were collected at the same rate using an analog data acquisition system integrated with the DIC unit. Therefore, stress-strain curve for every single point on the specimen can be obtained after analysis.

4.3.2.1 Theory of EWF calculation using DIC

At least three different patterns of deformation may be observed in different locations of a ductile DENT specimen during a destructive tensile test:

1. The points far away from the ligament (Figure 23) do not experience stress concentrations and therefore throughout the test are subjected to deformation within the elastic region. When the ligament fails and the stress in the region drops to zero, the deformations in these points are fully recovered. No energy is dissipated in these points.
2. The points close enough to the ligament to be affected by the related stress concentration but not on the fracture plane may experience stress levels above the yield limit and be subjected to plastic deformation. In these points certain amount

of deformation energy will be used to perform the irrecoverable work of plastic deformation.

3. The points along the ligament are assumed to form the fracture plane. In these points the deformation energy is first dissipated to perform the irrecoverable work of plastic deformation and then to create the fracture. This last component is referred to as the essential work of fracture.

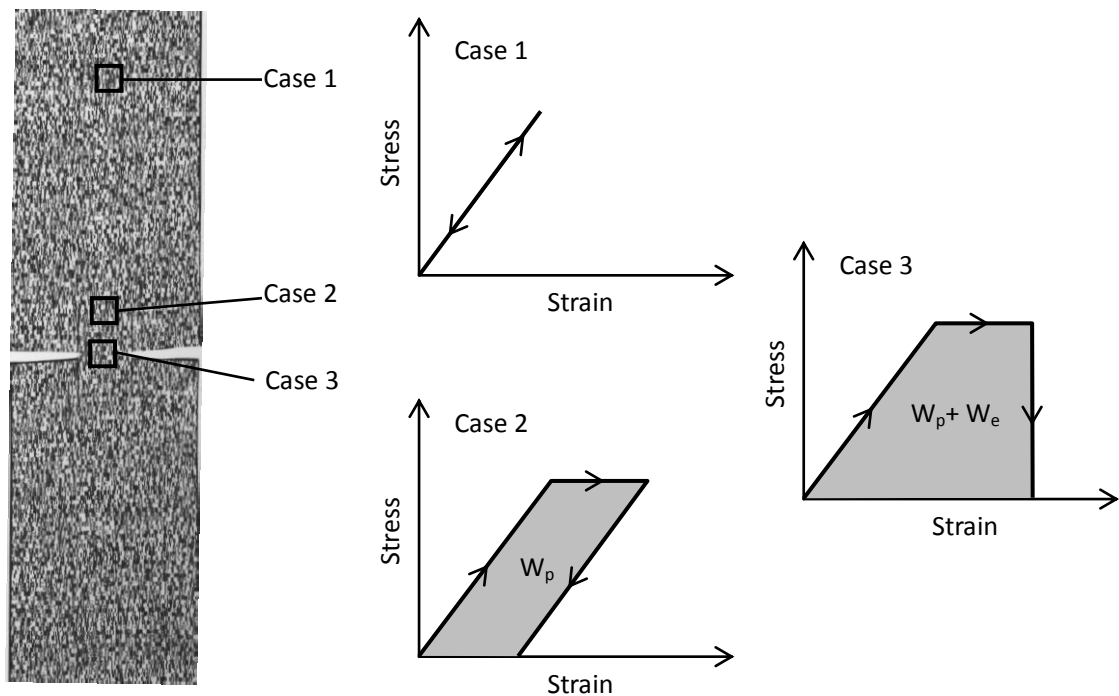


Figure 23. Three types of deformation in a DENT sample in tension: case 1, elastic deformation for points far away from the ligament; case 2, plastic deformation for points within the plastic deformation zone; case 3, plastic deformation and fracture for points along the ligament.

The optical measurement system returns strain values for thousands of regularly spaced reference points on the specimen surface. For each of such points on a specimen in tension, a curve of nominal stress vs. local strains can be obtained. Figure

24 shows the nominal stress vs. local strain curves at two different locations: one close to ligament and the other one far away from the ligament. These curves agree with the theoretical prediction very well.

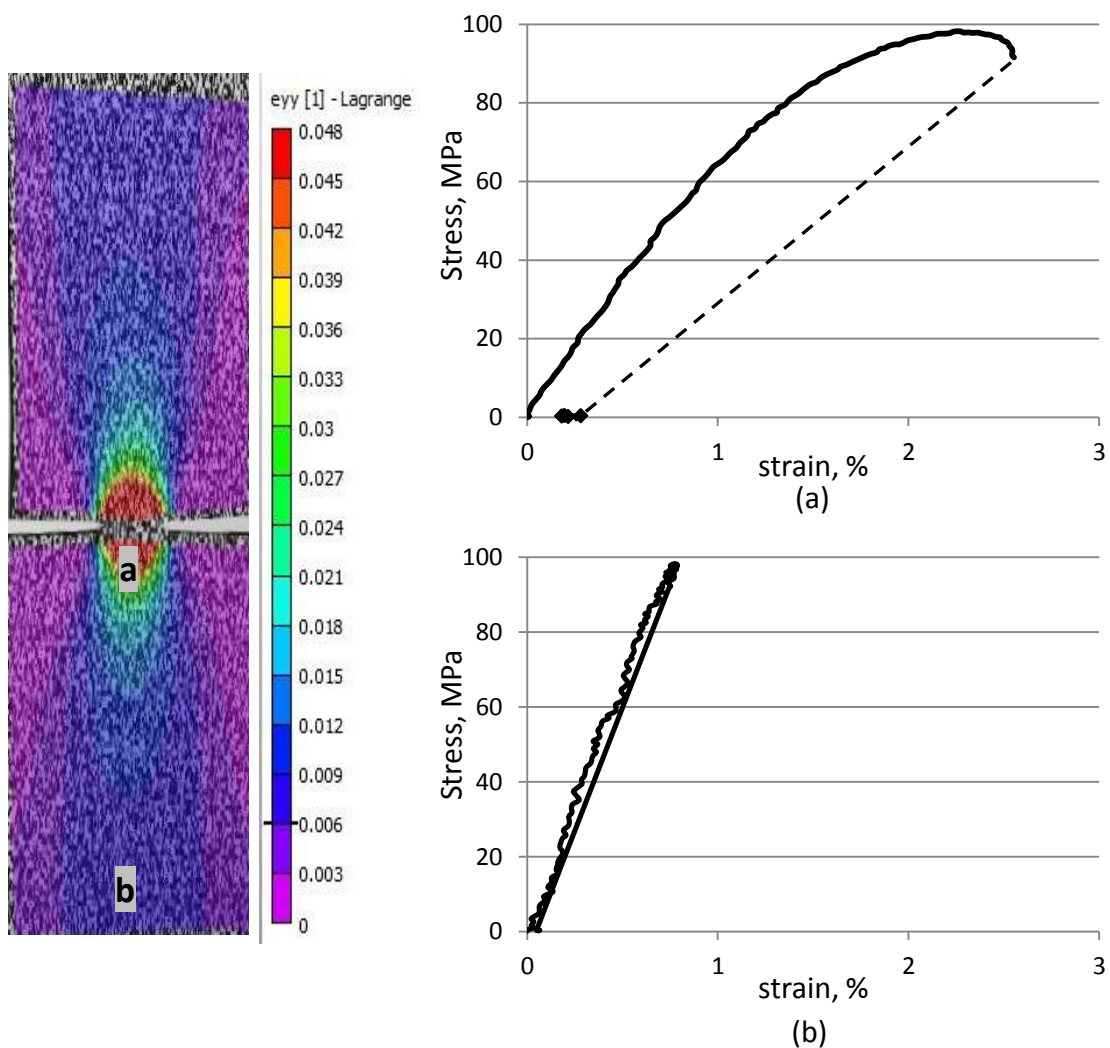


Figure 24. Left: Typical strain map of a DENT specimen just before failure; Right: nominal stress vs. local strain curves at location a (within plastic deformation zone) and b (elastic deformation zone)

In Figure 24a, it seems that initial elastic modulus was higher than recovery modulus.

In the matter of fact, there was no information between the point at the maximum

strain and the first point after failure. Therefore, we can not take the slope of the linear line between these two points as recovery modulus.

Figure 24b shows the slope of the elastic portion of stress-strain curve of point b was very high. It is because the stress was nominal stress, which was calculated based on cross section of ligament. Therefore, the stress was overestimated here. However, this estimation does not affect the measurement of plastic deformation, because as seen in Figure 25, plastic deformation is limited within the area near the ligament. All the plastic deformation outside the circle shown in Figure 25 can be ignored.

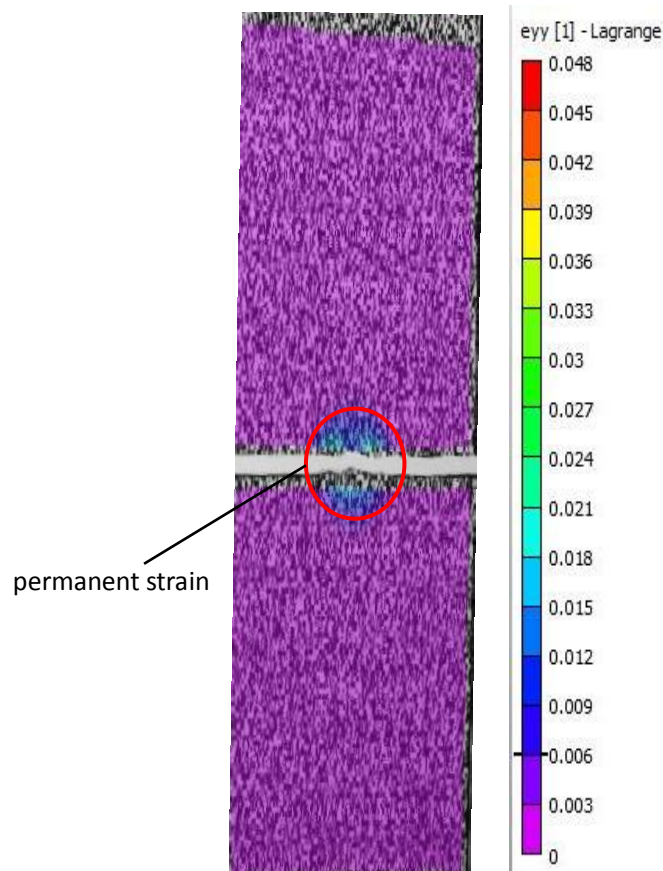


Figure 25. Strain mapping of a specimen after failure

The area under the curve is equivalent to the specific energy (energy per unit volume) consumed for plastic deformation and fracture at this location. From the records of strains, for thousands of points, the same scheme can be used to calculate the total work of plastic deformation. See schematic illustration of this process is shown in Figure 26. $\varepsilon_{\max j}$ is the maximum strain at point A_j , and $\sigma_{\max j}$ is the stress at $\varepsilon_{\max j}$. $\Delta\varepsilon_k$ indicates the k^{th} increase of strain starting from zero, and σ_k is the average stress at the k^{th} strain increase. ε_p represents the permanent strain at point A_j . Then the essential work of fracture (EWF) is calculated by subtracting the total work of plastic deformation from the total work to failure.

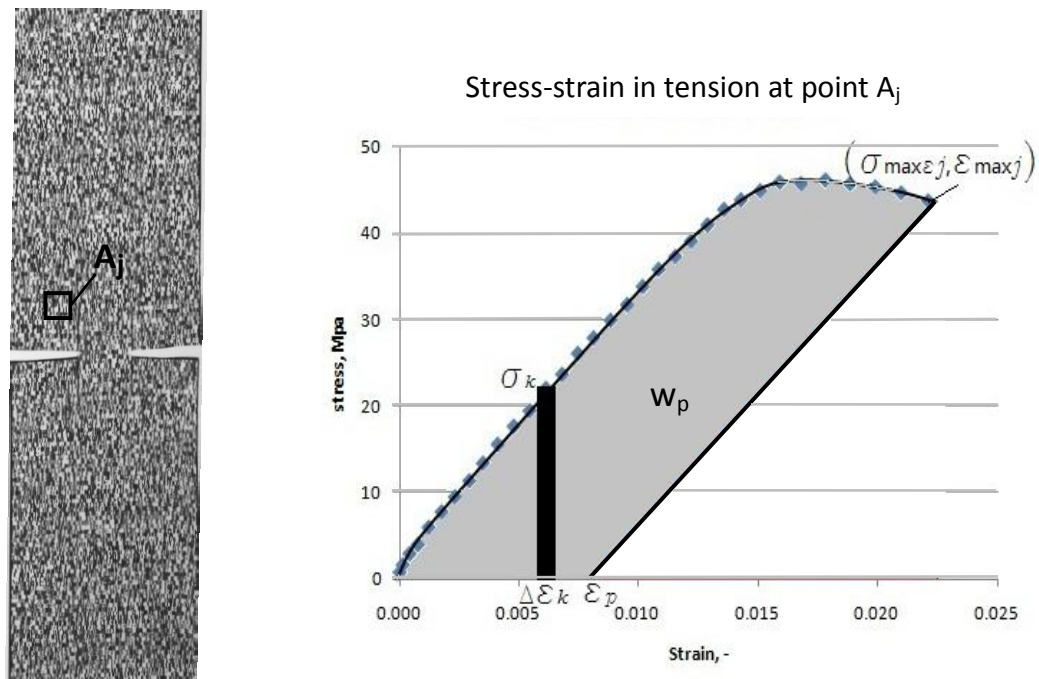


Figure 26. Typical stress-strain curve for a point A_j .

As illustrated above, total work to failure can be expressed as sum of work consumed for elastic deformation (always 0), plastic deformation and fracture :

$$\begin{aligned}
 W_T &= W_{el} + W_p + W_e \\
 &= 0 + W_p + W_e \\
 &= \int_V w_p dV + \int_A w_e dA = t \int_A w_p dA + w_e l t
 \end{aligned} \tag{7}$$

Where

W_{el} -total work for elastic deformation, [J]. It is always 0, because the elastic deformation is fully recoverable after the specimen is fractured.

W_p - total work for plastic deformation, [J]

W_e - total work for essential work of fracture, [J]

w_e - specific essential work of fracture, [J/m²]

w_p - specific work of plastic deformation [J/m³]

l - ligament length, [m]

t - thickness of specimen, [m]

V - volume of specimen, [m³]

A - area of specimen subjected to deformation, or AIO [m²]

Subareas ΔA_j outside the immediate fracture plane do not experience fracture but undergo certain amount of irreversible plastic deformation. The work of plastic deformation for each subarea ΔA_j may be calculated as the area bordered from the top by the stress-strain curve and the area from the bottom by the elastic recovery

curve following the stress release after the fracture (Figure 26.).

Then equation (7) becomes:

$$\begin{aligned}
 w_e l t &= W_T - t \int_A w_p dA \\
 &= \sum_i F_i \Delta \delta_i - t \Delta A_j \sum_j [\sum_k \sigma_k \Delta \varepsilon_k - \frac{1}{2} (\varepsilon_{maxj} - \varepsilon_{pj}) \sigma_{maxj}]
 \end{aligned} \tag{8}$$

Where

$\Delta \delta_i$ - i^{th} increasement of displacement starting from zero, [m]

F_i - the average load at the i^{th} strain increasement, [N]

ε_{maxj} - the maximum strain at point A_j

σ_{maxj} - the stress at ε_{maxj} , [Pa]

$\Delta \varepsilon_k$ - the k^{th} increasement of strain starting from zero

σ_k - the average stress at the k^{th} strain increasement, [Pa]

ε_p - the permanent strain point A_j .

The first term $\sum_i F_i \Delta \delta_i$ is obtained from force-displacement curve measured on the entire specimen, and the second term is obtained from all the stress-strain curves for all the subareas ΔA_j 's.

For regularly spaced points in the DIC area of interest, all subareas ΔA_j are equal and their size is determined by the step-size $\Delta A_j = \Delta A = d_{ss}^2$.

Where d_{ss} is step-size, a parameter of DIC analysis described in 4.2.2.1. It is in the unit of m.

Therefore, the essential work of fracture for the entire sample can be obtained as:

$$W_e = \frac{\sum_i F_i \Delta \delta_i - t d_{ss}^2 \sum_j [\sum_k \sigma_k \Delta \varepsilon_k - \frac{1}{2} (\varepsilon_{maxj} - \varepsilon_{pj}) \sigma_{maxj}]}{lt} \quad (9)$$

However, equation (9) can be simplified by replacing stress and strain for every individual point with stress and average strain over the entire area of interest (AOI). Only one stress vs. average strain curve is need to calculate EWF and the formula becomes:

$$W_e = 0.5 \sigma_{max\varepsilon} (\bar{\varepsilon}_{max} - \bar{\varepsilon}_p) \frac{A}{l} \quad (10)$$

Where

$\sigma_{max\varepsilon}$ - stress at maximum average strain over the AOI, [Pa]

$\bar{\varepsilon}_{max}$ - average strain over the AOI

$\bar{\varepsilon}_p$ - average permanent strain over the AOI

A - area of AOI, [m²]

l - ligament length, [m]

Discussion of equivalency of equation (9) and equation (10) is shown in Appendix B.

All the parameters in above equation (10) can be measured or calculated, and the

Matlab code of this algorithm is in Appendix C.

4.3.3 Expected Output and Measured Quantities

The procedures described in the previous sections yielded the following sets of data:

- Measurements dimensions including thickness and ligament length of each DENT specimen were manually tabularized.
- Load and positions of crosshead of Instron for each tensile test were recorded at the rate of 10 measurements per second with the data acquisition unit integrated with the testing machine and saved in comma-separated-value (.csv) text files available for further processing.
- The optical measurement (DIC) system collected the time-stamped images of the deformed specimens recorded simultaneously by the two cameras at the various rate of 1 to 6 per second, depending on ligament length or testing duration. In general, about 150 pairs of images were acquired for each test. The corresponding loads and displacements measured with the Instron testing machine were probed at the same rate using an analog data acquisition system integrated with the DIC unit. The time stamps and recorded analog data have been saved in comma-separated-values (.csv) text files available for further processing.

4.3.4 Data Treatment

EWf of polyester films were calculated using two methods: traditional experimental method described in literature (Saleemi and Nairn 1990) and the method based on optical measurement using DIC as described above.

4.3.4.1 EWF calculated from traditional experimental method

According to Equation (4) $\frac{W_T}{lt} = w_t = w_e + \beta w_p l$, essential work of fracture w_e is determined by the intercept of the best linear fit at zero ligament length. Total work to failure W_T was obtained by computing the area under force-displacement curve. W_T was then divided by cross-sectional area of ligament (lt) to obtain w_t . Then w_t was plotted against ligament length l . Finally the intercept of the linear regression line at zero ligament length were determined.

4.3.4.2 EWF calculated from method based on optical measurement using DIC

Essential work of fracture w_e was calculated follow the steps described in section 4.3.2.1.

4.3.5 Verification of the alternative method of EWF measurement

Essential work of fracture (EWF) of polyester films measured by two methods, traditional method as described in (Saleemi and Nairn 1990) and method based on optical measurement using DIC, are reported and compared to verify the alternative method of EWF measurement.

4.3.5.1 EWF measured using traditional method

Typical load-displacement curves for all the seven ligament-length groups were plotted in one diagram. See Figure 27.

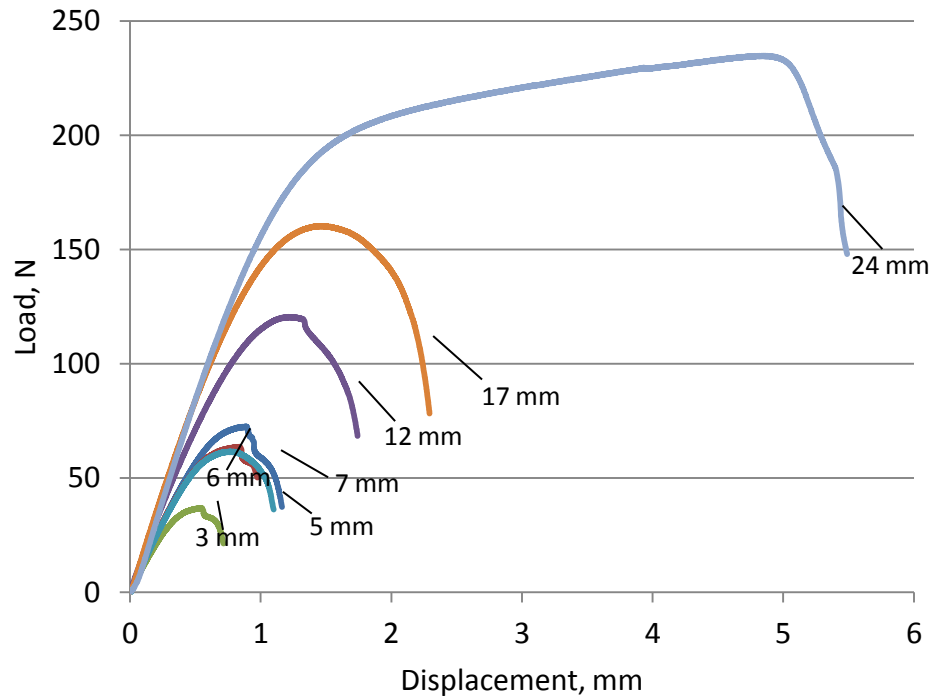


Figure 27. Typical load-displacement curves for all the seven ligament-length groups

Total work to failure W_t of each specimen was measured by calculating the area under its load-displacement curve. W_t was then divided by cross-sectional area of ligament (lt) to obtain specific work to failure w_t . Average w_t of each ligament-length group against ligament length was plotted in Figure 28.

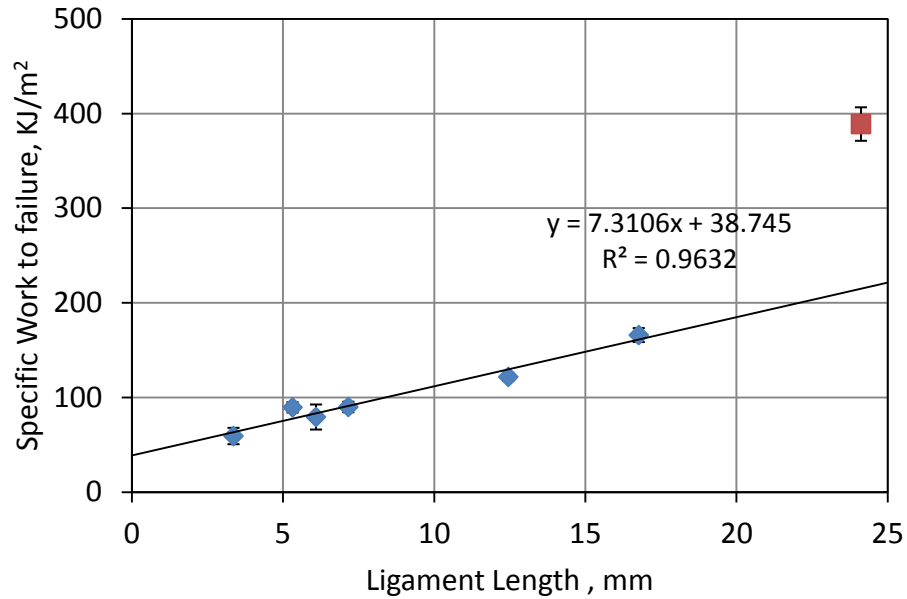


Figure 28. Specific work to failure w_t as a function of ligament length l

Saleemi and Nairn suggested that the ligament length should be smaller than $1/3$ of the width of a specimen (Saleemi and Nairn 1990). Their studies also showed that for long ligament lengths ($l > W/3$), the specific work to failure reached a plateau. Our result showed that the specific work to failure w_t and ligament length l had good linear relationship ($R^2 = 0.9632$) up to $l = 17$ mm, which is about $2/3$ of the width. w_t obtained from ligament length $l = 24$ mm was much higher than the regression line calculated for the other six data sets.

Since the ligament lengths were much larger than the thickness of specimens, i.e., $l > (3 - 5)t$ at all cases, the intercept of the linear regression line at zero ligament length gave a plane-stress essential work of 38.7 KJ/m^2 . The slope of the linear regression line gave $\beta w_p = 7.31 \text{ MJ/m}^3$.

4.3.5.2 EWF measured using optical measurement

All the DENT specimens for measuring EWF were divided into three groups according to ligament length: ligament length less than $W/3$, ligament length larger than $W/3$ and unnotched ($l = W$). EWF calculated using algorithm described in section 4.3.2.1 for each group of specimens are compared in Figure 29 and Table 10.

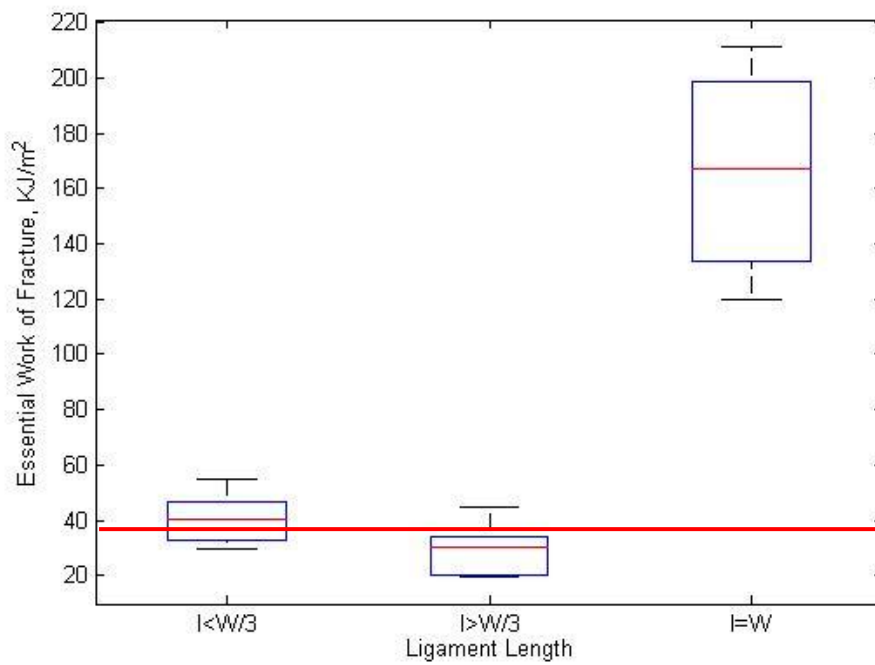


Figure 29 Comparison of EWF measured using optical measurement for three groups of DENT specimens

Table 10. EWF measured from three groups of DENT specimens and determined by John Nairn's Method

	$l < W/3$	$l > W/3$	$l = W$	Nairn's method
Average EWF, KJ/m ²	40.8	29.3	166	38.7
COV, %	19.2	32.0	24.3	-

The average EWF calculated using optical measurement for the group of $l < W/3$ was 40.8 KJ/m², which matched the value (38.7 KJ/m²) determined by traditional method very well (t -test: p -value=0.2640 at 95% confidence level). However, the average EWF for the group of $l > W/3$ was only 29.3 KJ/m², which was 24% lower than the value determined by traditional method. They were statistically significantly different (t -test: p -value=0.0011 at 95% confidence level).

The average EWF of unnotched specimens was 166 KJ/m². It was much higher than the EWF obtained by traditional method.

Therefore, as long as the ligament length of DENT specimens is less than 1/3 of the width, this new method can be used to evaluate reliable EWF of a material by a test on one specimen. This method can not be used to evaluate EWF from simple tensile tests on unnotched specimens used to determine the tensile strength, elastic modulus, Poisson's ratio and toughness (specific work to failure). However, a reasonably accurate measurement of EWF is possible if a small set of notched specimens can be produced from the prototype samples.

5. RESULTS AND DISCUSSION

In this chapter, SEM micrographs of two types of freeze-dried MFC aerogel samples were presented, and morphological characteristics of the aerogel samples were described. Then mechanical properties of bulk MFC-PLA nanocomposite films were reported.

5.1 Morphological characterization of MFC

Freeze-dried aerogel samples made from two types of MFC, type A from University of Maine and type B from Innventia AB company, were investigated under SEM. Three series of SEM micrographs at various magnification levels were generated for each type of sample.

Representative SEM micrographs of freeze-dried aerogel samples from two types of MFC are presented in Figure 32 and Figure 33. More SEM micrographs can be seen in attached CD (see description in Appendix D).

Degree of fibrillation (DOF) is used to evaluate how well the material is fibrillated. If the MFC aerogel is fully fibrillated, i.e., it is composed of distinct nano-sized fibers or particles and there is no agglomeration observed, the DOF is 1. On the contrary, if there is no existence of nano-sized fibers or particles in the material, the DOF is considered as 0.

Two types of MFC aerogels were also compared at same magnification levels in Figure 31. Both materials were not fully fibrillated and showed complex hierarchical structure that cannot be described in terms of quantifiable morphological descriptors commonly used to characterize particulate matter or cellular structures. Unlike typical fibers, they cannot be simply described in terms of aspect ratio or sphericity, since the nanofibers were aggregated in the form of flakes. Similarly, the descriptors used for cellular structures (e.g. sponge (Figure 30)), which are usually described by number of faces, edges and vertices (nodes), as well as thickness and relative length of edges are of little help here. Obviously, these descriptors are not adequate to describe the morphology of either type A nor type B MFC.

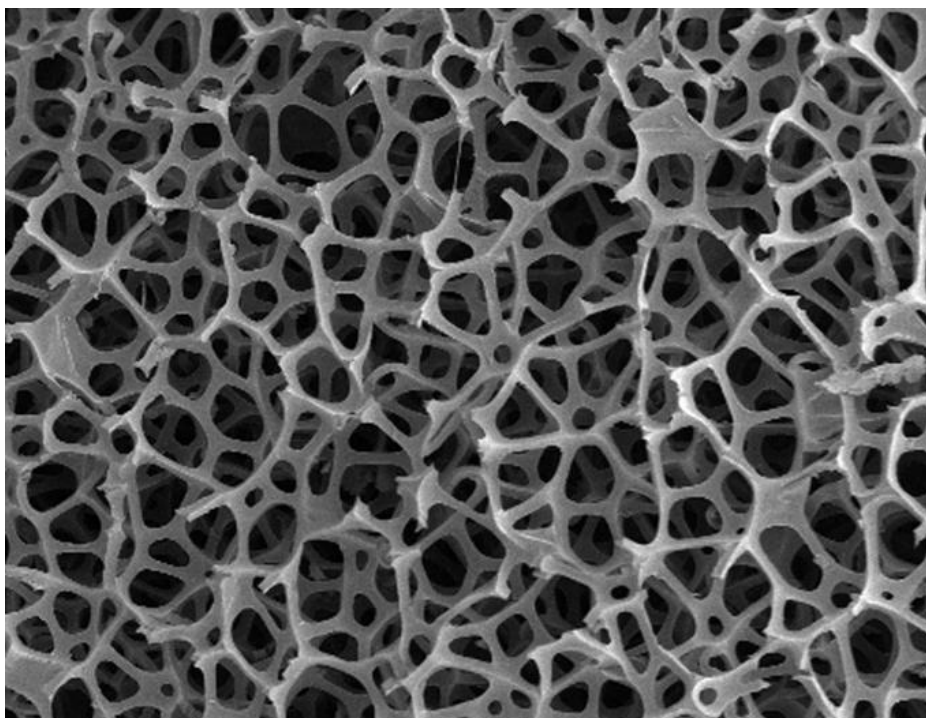


Figure 30. Microstructure of a dry sponge swab (Carr 2007)

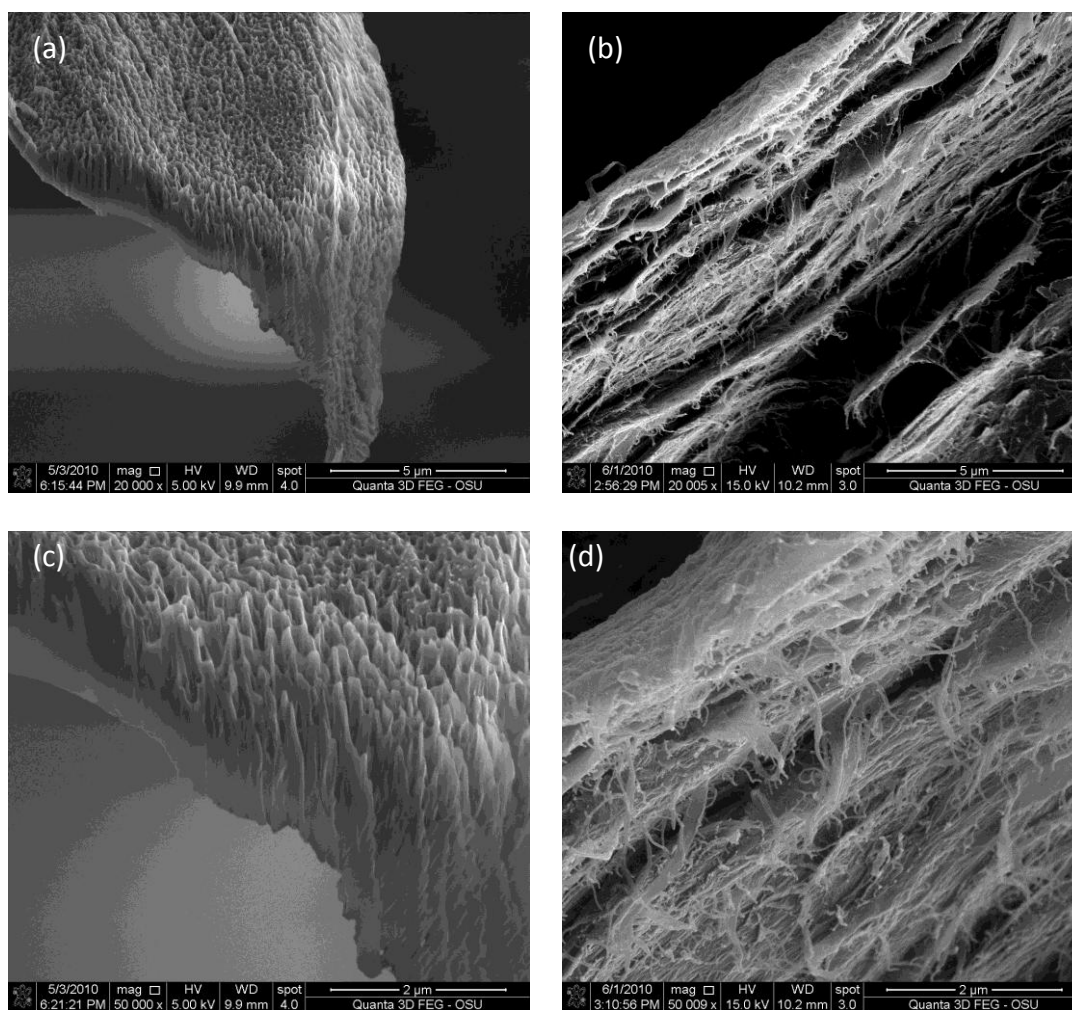


Figure 31. Structure and appearance of MFC by SEM a) type A MFC, 20 000X; b) type B MFC, 20 000X; c) type A MFC, 50 000X; d) type B MFC, 50 000X

Sample SEM micrographs of type A MFC aerogel at different levels of magnification are shown in Figure 32.

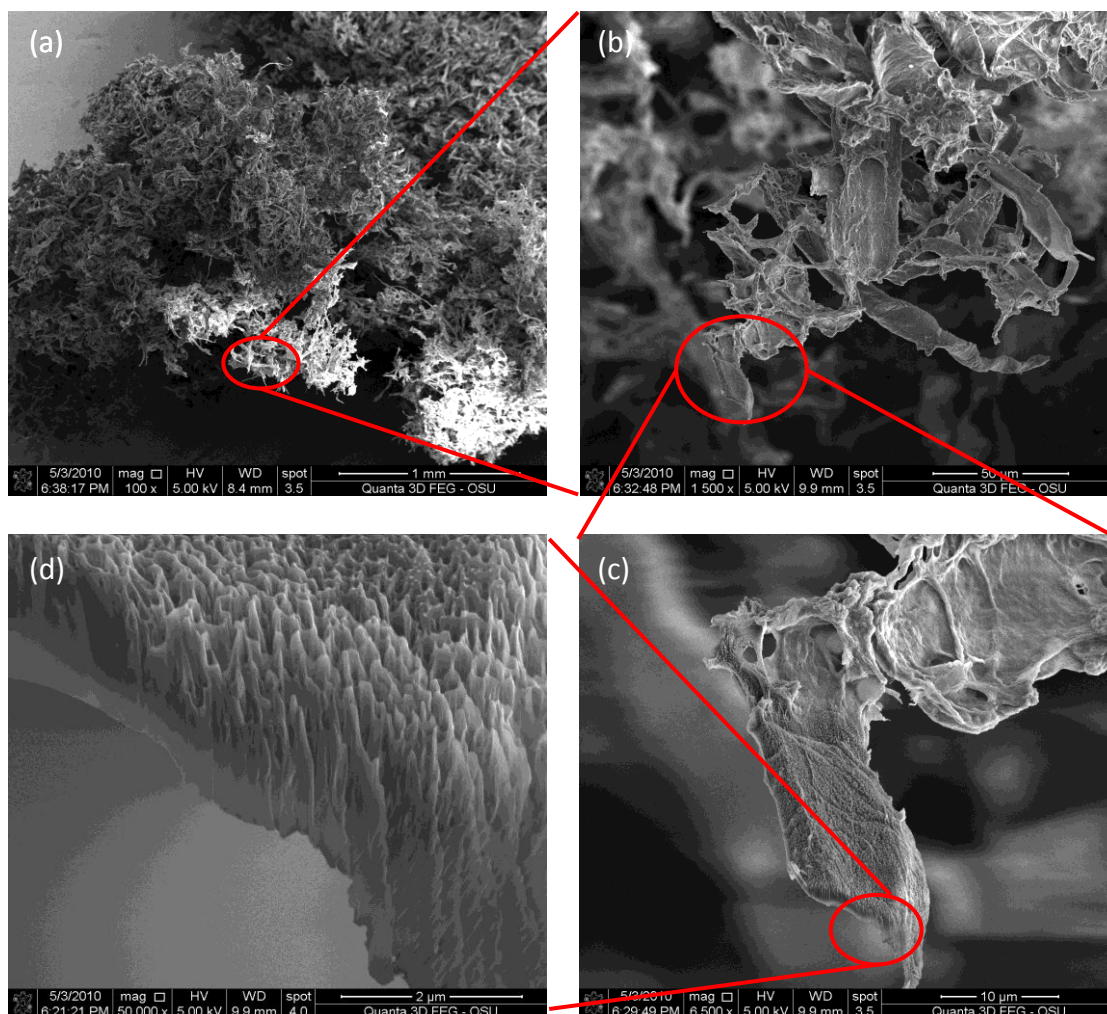


Figure 32. SEM micrographs of type A MFC aerogel at different levels of magnification: (a) 100 X; (b) 1500X; (c) 6500 X (d)50,000 X

At low level of magnification (Figure 32a and b), type A MFC aerogel was composed of various irregular-shaped leaf-like flakes. As seen in the detailed image of the flakes (Figure 32d), the structure of flakes was like carved hoodoos. Individual cellulose nanofibers cannot be recognized from the SEM micrographs, even at highest magnification (50,000 X). It seems that DOF of Type A MFC was about 0.

Sample SEM micrographs of type B MFC aerogel at different levels of magnification are showed in Figure 33.

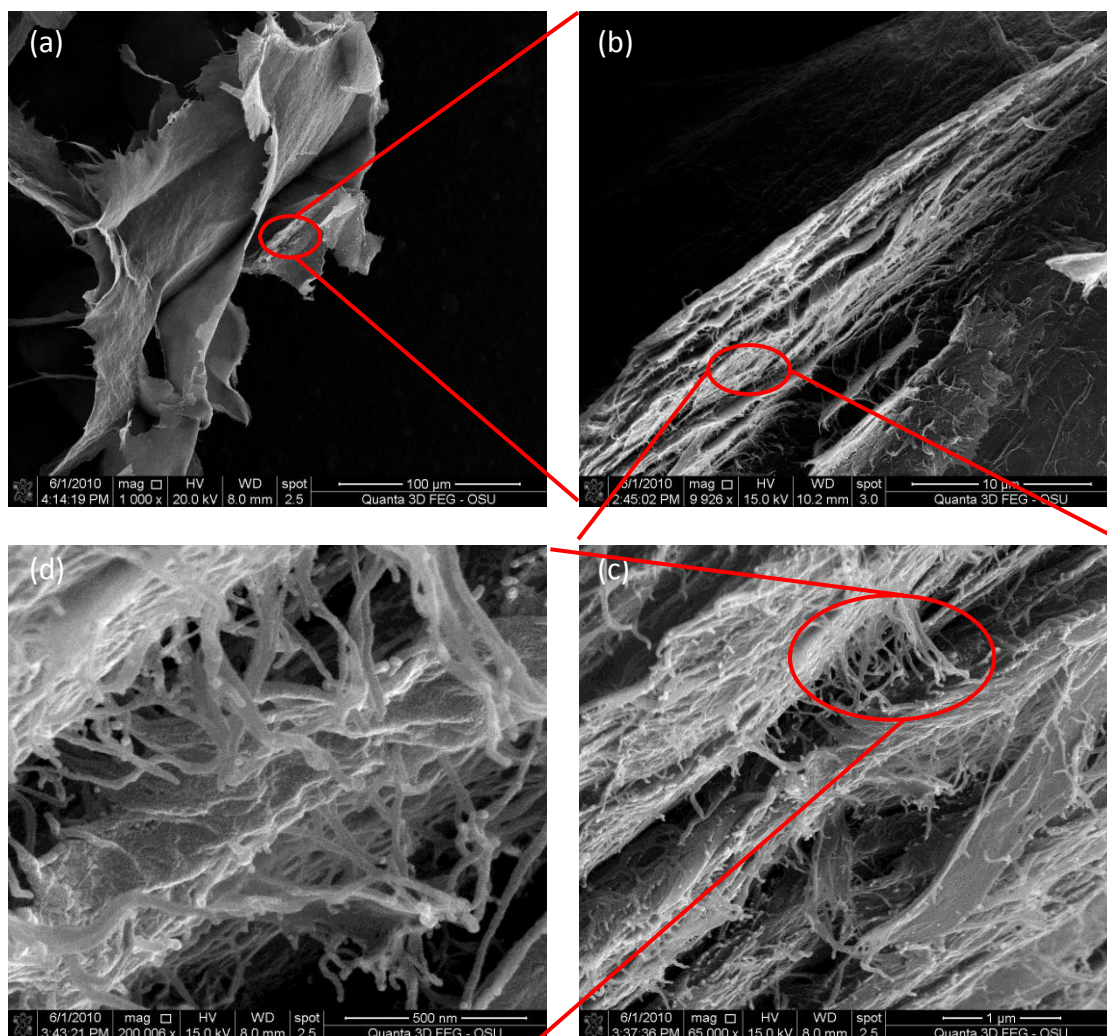


Figure 33. SEM micrographs of type B MFC aerogel at different levels of magnification:

(a) 1000 X; (b) 10,000X; (c) 65,000 X (d) 200,000 X

As seen in the image at low magnification level (Figure 33a), type B MFC aerogel consisted of conglomerated flakes. Close-up image of a flake (Figure 33b) shows it was composed of multiple layers. Spike-like individual cellulose nanofibers could be

recognized with one end embedded in the layer (Figure 33c and d). These nanofibers were in the width of ~ 30 nm, and they could be considered as better fibrillated than MFC A (Figure 31). However, it is impossible to measure the length of MFC from these SEM micrographs, and therefore the aspect ratio of the fibrils cannot be evaluated.

5.2 Mechanical characterization of bulk MFC-PLA nanocomposites

Mechanical properties of bulk MFC-PLA nanocomposite films were determined. These include: tensile strength, elastic modulus, toughness (expressed as specific work to failure) and Poisson's ratio. In order to obtain reliable measurement of elastic modulus and toughness, strains in the specimens were calculated from optical measurement based on DIC.

5.2.3 Mechanical properties of MFC-PLA nanocomposite films

Tensile strength, elastic modulus, toughness (expressed as the specific work to failure) and Poisson's ratio of bulk MFC-PLA nanocomposite films reinforced by two types of MFC are reported in this section. Strains were calculated based on "virtual extensometer" (method c described in section 4.2.4.2), because this method simulates measurement with a conventional extensometer. It may be used for comparisons with published data.

Table 11 and Figure 34 to Figure 36 summarize the mechanical properties of MFC-PLA nanocomposite films with type A MFC. Symbols UT and LT in legend represent untreated and lactide treated respectively. Numbers in the brackets are standard deviations for each group of tests.

Table 11. Tensile strength, elastic modulus, toughness and Poisson's ratio of MFC-PLA nanocomposites with type A MFC

	MFC loaded	Tensile Strength MPa	Elastic Modulus GPa	Toughness MJ/m ³	Poisson's Ratio
Reference	0%	46.8 (2.96)	2.98 (0.28)	1.31 (0.27)	0.29 (0.01)
Untreated MFC	0.10%	44.7 (5.62)	2.72 (0.26)	0.61 (0.11)	0.30 (0.03)
	0.25%	44.2 (3.53)	2.64 (0.27)	0.60 (0.11)	0.30 (0.02)
	0.50%	49.2 (2.57)	3.09 (0.14)	0.55 (0.06)	0.29 (0.01)
Lactide Treated MFC	0.10%	48.3 (2.35)	2.91 (0.06)	0.62 (0.17)	0.33 (0.05)
	0.25%	45.0 (3.23)	2.69 (0.31)	0.67 (0.17)	0.22 (0.05)
	0.50%	43.6 (3.54)	2.79 (0.11)	0.63 (0.27)	0.28 (0.03)

Note: MFC loading levels were based on weight percent.

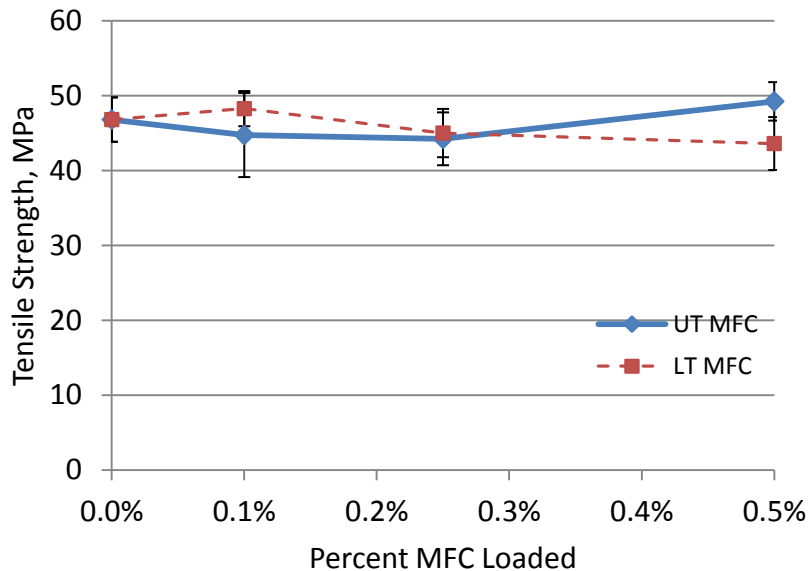


Figure 34. Tensile strength as a function of type A MFC loading levels for (by weight) MFC-PLA nanocomposite films with untreated MFC and lactide treated MFC

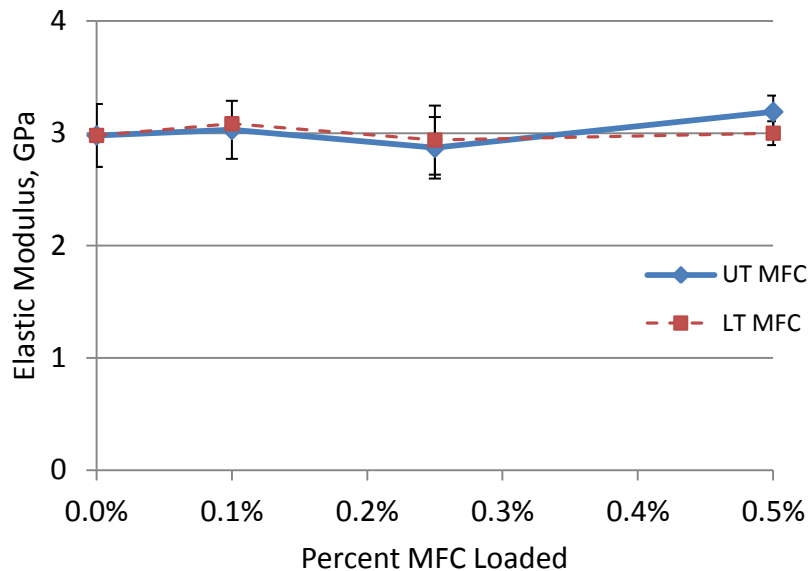


Figure 35. Elastic modulus as a function of type A MFC loading levels (by weight) for MFC-PLA nanocomposite films with untreated MFC and lactide treated MFC

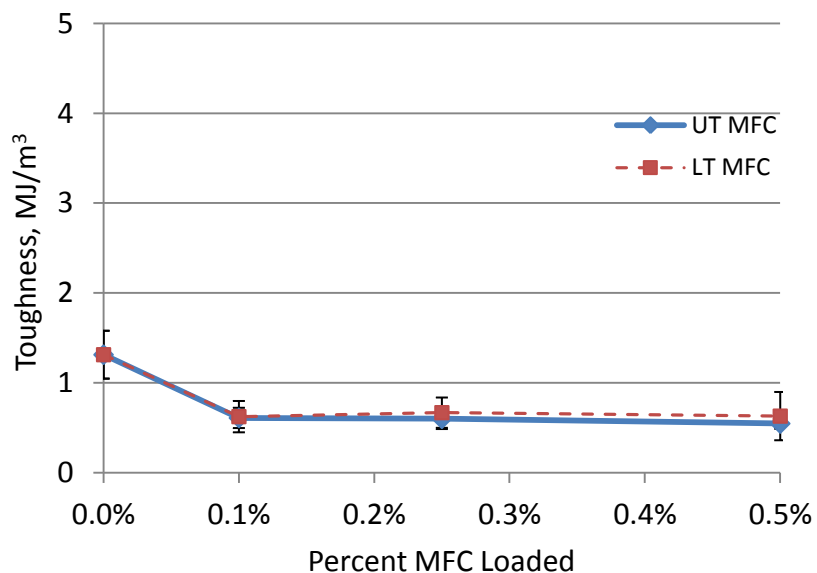


Figure 36. Toughness as a function of type A MFC loading levels (by weight) for MFC-PLA nanocomposite films with untreated MFC and lactide treated MFC

The tensile strength of neat PLA film was 46.8 MPa. As the loadings of untreated type A MFC were 0.10 and 0.25 wt%, the tensile strength of MFC-PLA films decreased by

4.5 and 5.6% respectively. However, as the loading of untreated type A MFC reached to 0.50 wt%, the tensile strength increased by 5.1% compared to that of neat PLA film. For MFC-PLA films with lactide treated type A MFC, the tensile strength increased by 3.2% with the MFC loading of 0.10 wt%, but decreased by 3.8% and 6.8% with the MFC loading of 0.25 and 0.50 wt% respectively. However, none of these effects was significant at 95% confidence level.

The elastic modulus of neat PLA film was 2.98 GPa. As the loadings of untreated type A MFC were 0.10 and 0.25 wt%, the elastic modulus of MFC-PLA films decreased by 8.7 and 11.4% respectively. However, as the loading of untreated type A MFC reached to 0.50 wt%, the elastic modulus increased by 3.7% compared to that of neat PLA film. For MFC-PLA films with lactide treated type A MFC, the elastic modulus decreased by 2.3, 9.7 and 6.4% with the MFC loading of 0.10, 0.25 and 0.50 wt%, respectively. Again none of these effect was significant at the 95% confidence level.

The toughness of neat PLA film measured as the total work to failure was 1.31 MJ/m³. However, the toughness of both MFC-PLA films with untreated and lactide treated type A MFC dropped to around 0.6 MJ/m³ at MFC loading level of 0.10 wt% and remained at the same level with the MFC loading level increased up to 0.50%.

Table 12 and Figure 34 to Figure 36 summarize the mechanical properties of MFC-PLA nanocomposite films with type B MFC. The loading levels were 5%, 10% and 15% for

both untreated and lactide treated MFC.

Table 12. Tensile strength, elastic modulus, toughness and Poisson's ratio of MFC-PLA nanocomposites with type B MFC

	MFC loaded	Tensile Strength MPa	Elastic Modulus GPa	Toughness MJ/m ³	Poisson's Ratio
Reference	0%	40.2 (9.24)	1.27 (0.35)	3.02 (1.83)	0.29 (0.02)
Untreated MFC	5%	13.8 (5.78)	0.46 (0.19)	0.27 (0.15)	0.31 (0.03)
	10%	22.3 (8.19)	0.62 (0.24)	0.89 (0.63)	0.32 (0.02)
	15%	20.25 (2.57)	0.64 (0.17)	1.28 (1.30)	0.29 (0.03)
Lactide Treated MFC	5%	8.18 (4.94)	0.33 (0.21)	0.11 (0.07)	0.32 (0.02)
	10%	9.28 (4.22)	0.48 (0.30)	0.11 (0.04)	0.32 (0.03)
	15%	22.2 (11.7)	0.87 (0.24)	0.39 (0.37)	0.30 (0.05)

Note: MFC loading levels were based on weight percent.

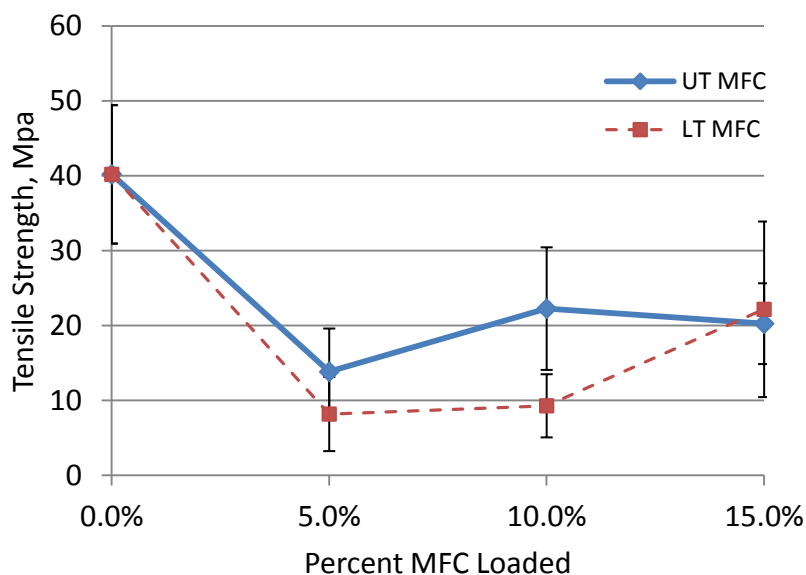


Figure 37. Tensile strength as a function of type B MFC loading levels (by weight) for MFC-PLA nanocomposite films with untreated MFC and lactide treated MFC

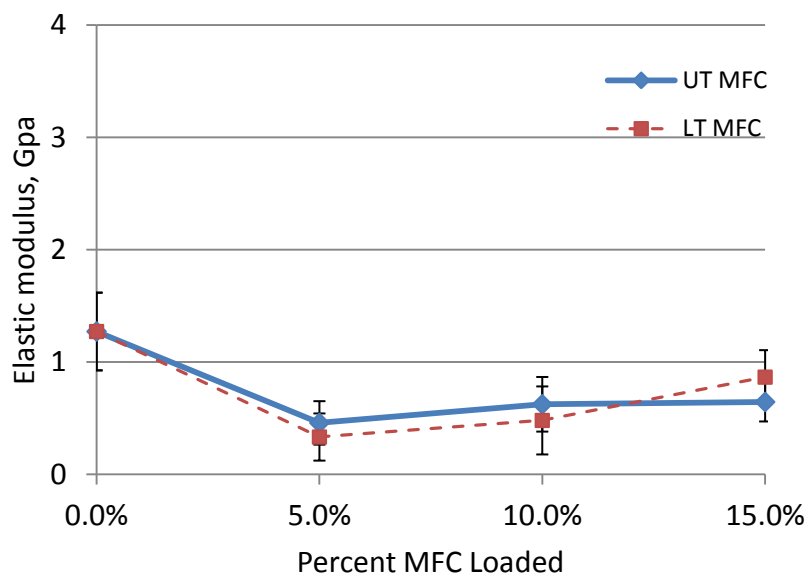


Figure 38. Elastic modulus as a function of type B MFC loading levels (by weight) for MFC-PLA nanocomposite films with untreated MFC and lactide treated MFC

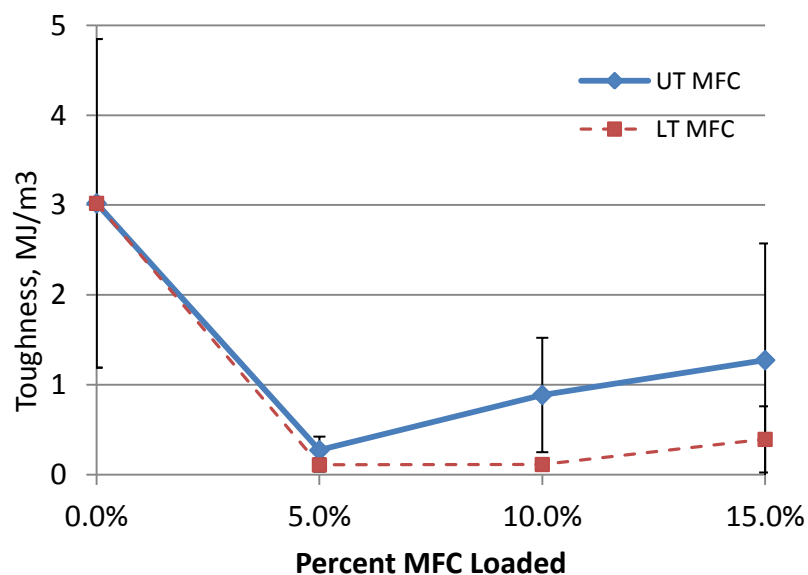


Figure 39. Toughness as a function of type B MFC loading levels (by weight) for MFC-PLA nanocomposite films with untreated MFC and lactide treated MFC

The tensile strength, elastic modulus and toughness of this batch of neat PLA films were 40.2 MPa, 1.27 GPa and 3.02 MJ/m³, respectively. The reason why the properties of the neat PLA films appeared different from those listed in Table 11 was probably that this batch of PLA films had higher porosity than previous batch. Porosity control is one of the biggest issues during the PLA and PLA composite film prototype manufacturing processing. Porosity may vary largely from batch to batch if film casting is not properly processed. Here we compared mechanical properties of neat PLA film samples and MFC-PLA composite film samples within batch.

For MFC-PLA films with untreated type B MFC, tensile strength dropped by 65.5% at MFC loading level of 5.0 wt%. Then it increased up to 22.3 MPa at MFC loading level of 10.0 wt%, and there was no significant change at 15.0 wt% loading level. For MFC-PLA films with lactide treated type B MFC, tensile strength dropped by 79.7% at MFC loading level of 5.0 wt%. However, it increased up to 22.2 MPa at 15.0 wt% loading level.

Elastic modulus of MFC-PLA films with untreated type B MFC decreased by 63.8% at MFC loading level of 5.0 wt%. Then as MFC loading level reached to 15 wt%, the value increased up to 48.9% of the elastic modulus of neat PLA film. Elastic modulus of MFC-PLA films with lactide treated type B MFC had very similar values as those of films with untreated type B MFC at each loading level.

Toughness of MFC-PLA films with untreated type B MFC decreased by 91.1% at MFC loading level of 5.0 wt%. Then as MFC loading level reached to 15 wt%, this value increased up to 42.4% of the toughness of neat PLA film. Toughness of MFC-PLA films with lactide treated type B MFC decreased by 96.4% at MFC loading level of 5.0 wt%. As MFC loading level reached to 15 wt%, this value increased to 12.9% of the toughness of neat PLA film.

6 CONCLUSIONS

The morphology of the two analyzed MFC types was complex. The microscopic structure of the MFC aerogels appeared as a combination of nanofibers and flakes. Although the thickness of individual nanofibers could be measured, the hierarchical structures we investigated did not allow qualitative characterization of the morphological features in terms of particulate composites nor cellular solids.

An optical measurement method based on DIC has been successfully developed to measure strains in transparent thin films, which allowed determination of the critical mechanical properties including tensile strength, elastic modulus, Poisson ratio, and toughness (expressed as specific work to failure) from the same set of specimens subjected to tensile tests. In our study, the accuracy and precision of the measurement of deformation were $\pm 1.5 \mu\text{m}$ and $0.4 \mu\text{m}$ respectively. The corresponding accuracy and precision in terms of strains were $\pm 30 \mu\text{strain}$ and $75 \mu\text{strain}$ respectively. Such high accuracies and precisions of deformations and strains enable optical measurement method based on DIC principle to be a robust method of measuring deformations and strains for thin transparent film samples.

The attempt to measure the EWF from the same tensile tests was not successful. Another set of specimens has to be produced in order to measure this property.

However, the optical measurement method can significantly simplify the testing for measuring EWF of thin transparent films. This method requires smaller number of notched specimens than traditional method described by John Nairn et al.

BIBLIOGRAPHY

- Andresen, M., L. S. Johansson, et al. (2006). "Properties and characterization of hydrophobized microfibrillated cellulose." Cellulose **13**(665-677).
- ASTM (2007). D5045: Standard Test Methods for Plane-Strain Fracture Toughness and Strain Energy Release Rate of Plastic Materials. West Conshohocken, PA, ASTM International.
- ASTM (2008). ASTM E 2655-08 Standard Guide for Reporting Uncertainty of Test Results and Use of the Term Measurement Uncertainty in ASTM Test Methods. West Conshohocken, PA, American Society for Testing and Materials.
- ASTM (2009). D 822-09: Standard Test Method for Tensile Properties of Thin Plastic Sheeting. West Conshohocken, PA, American Society for Testing and Materials.
- Barany, T., T. Caigany, et al. (2003). "Essential work of fracture concept in polymers." PERIODICA POLYTECHNICA SER. MECH. ENG. **47**(2): 91-102.
- Beck-Candanedo, S., M. Roman, et al. (2005). "Effect of reaction conditions on the properties and behavior of wood cellulose nanocrystal suspensions." Biomacromolecules **6**(2): 1048-1054.
- Braun, B., J. R. Dorgan, et al. (2008). "Cellulosic nanowhiskers. Theory and application of light scattering from polydisperse spheroids in the Rayleigh-Gan-Debye regime." Biomacromolecules **9**(4).
- Braun, B., J. R. Dorgan, et al. (2006). "Reactively Compatibilized Cellulose Polylactide Microcomposites." Journal of Polymers and the Environment **14**(1): 49-58.
- Carr, J. (2007). "Peering into the micro world." from <http://www.boston.com/bigpicture/2008/>.
- Cheng, Q. and S. Wang (2008). "A method for testing the elastic modulus of single cellulose fibrils via atomic force microscopy." Composites Part A: applied science and manufacturing **39**: 1838-1843.
- Dufresne, A., D. Dupeyre, et al. (2003). "Lignocellulosic flour-reinforced poly(hydroxybutyrate-co-valerate) composites." Journal of Applied Polymer Science **87**: 1302-1315.
- Eichhorn, S. J., A. Dufresne, et al. (2010). "Review: current international research into

cellulose nanofibres and nanocomposites " Journal of Materials Science **45(1)**: 1-33.

Elazzouzi-Hafraoui, S., Y. Nishiyama, et al. (2008). "The shape and size distribution of crystalline nanoparticles prepared by acid hydrolysis of native cellulose." Biomacromolecules **9**: 57-65.

Gallery. (2011). "Random-unpredictable, irregular and chance." 2011, from http://mirror-us-ga1.gallery.hd.org/_c/math/_more2004/_more10/random-dots-speckles-mono-bg-1-DHD.jpg.html.

Garlotta, D. (2001). "A Literature Review of Poly(Lactic Acid) " Journal of Polymers and the Environment **9(2)**: 63-84.

Gerlock, G. (2011). "Demand for bioplastics on the rise." Retrieved August 13, 2011, from <http://www.kvnonews.com/2011/07/demand-for-bioplastics-on-the-rise/>.

Glasbrenner, B. (2005). "NatureWorks® PLA – Commercial Development of Biopolymers on a World Scale " Technical Program for GPEC: 1-5.

Hartmann, M. H. (1998). Biopolymers from renewable resources. Berlin, Springer_Verlag.

Henriksson, M., G. Henriksson, et al. (2007). "An environmentally friendly method for enzyme-assisted preparation of microfibrillated cellulose (MFC) nanofibers." European Polymer Journal **43(8)**: 3434-3441.

Hubbe, M. A. and O. J. Rojas (2008). "Cellulosic nanocomposites: a review." Bioresources **3(3)**: 929-980.

Hung, P.-C. and A. S. Voloshin (2003). "In-plane Strain Measurement by Digital Image Correlation." J. of the Braz. Soc. of Mech. Sci. & Eng. **XXV(3)**: 215-221.

Ikeda, K., M. Takatani, et al. (2008). "Development of fully bio-based composite: Wood/cellulose diacetate/poly(lactic acid) composite." Holzforschung **62**: 154-156.

Iwatake, A., M. Nogi, et al. (2008). "Cellulose nanofiber-reinforced polylactic acid." Composites Science and Technology **68**: 2103-2106.

Juntaro, J., M. Pommet, et al. (2007). "Nanocellulose enhanced interfaces in truly green unidirectional fibre reinforced composites." Composite Interfaces **14**: 753-762.

Kroschwitz, J. I. (1990). Concise Encyclopedia of Polymer Science and Engineering. New York, John Wiley & Sons.

- Kvien, I. and K. Okaman (2007). "Orientation of cellulose nanowhiskers in polyvinyle alcohol." Applied physics A **87**: 641-643.
- Kvien, I. and B. S. Tanem (2005). "Characterization of cellulose whiskers and their nanocomposites by atomic force and electron microscopy." Biomacromolecules **6**: 3160-3165.
- Kwon, H. J. and P. Y. Jar (2007). "Application of essential work of fracture concept to toughness characterization of high-density polyethylene." Polymer Engineering and Science **47**(9): 1327-1337.
- Lagaron, J. M., R. Catala, et al. (2004). "Structural characteristics defining high barrier polymeric materials." Materials Science and Technology **20**: 1-7.
- Lemmouchi, Y., M. Perry, et al. (2007). "Novel synthesis of biodegradable star poly(ethylene glycol)-block-poly(lactide) copolymers." Journal of Polymer Science: Part A: Polymer Chemistry **45**: 3966-3974.
- Lindström, T., M. Ankerfors, et al. (2007). METHOD FOR THE MANUFACTURE OF MICROFIBRILLATED CELLULOSE. WO/2007/091942, STFI- PACKFORSK AB
- Liu, C.-H. and J. A. Nairn (1998). "Using the essential work of fracture method for studying physical aging in thin, ductile, polymeric films." Polymer Engineering and Science **38**(1): 186-193.
- Liu, D. Y., X. W. Yuan, et al. (2010). "Characterisation of solution cast cellulose nanofibre-reinforced poly(lactic acid)." eXPRESS Polymer Letters **14**(1): 26-31.
- Lu, H. and P. D. Cary (2000). "Deformation Measurements by Digital Image Correlation: Implementation of a Second-order Displacement." Experimental Mechanics **40**(4): 393-400.
- Martin, O. and L. Averous (2001). "Poly(lactic acid): plasticization and properties of biodegradable multiphase system." Polymer **42**(6209-6219).
- Mathew, A. P., K. Oksman, et al. (2005). "Mechanical Properties of Biodegradable Composites from Poly Lactic Acid (PLA) and Microcrystalline Cellulose (MCC)." Journal of Applied Polymer Science **97**: 2014-2025.
- MatWeb. (2011). "Material Property Data." Retrieved August 12, 2011, from <http://www.matweb.com>.
- Menezes, A. J. d., G. Siqueira, et al. (2009). "Extrusion and characterization of functionalized cellulose whiskers reinforced polyethylene nanocomposites." Polymer **50**: 4552-4563.
- Momani, B. (2009). Assessment of the impacts of bioplastics: energy usage, fossil fuel

usage, pollution, health effects, effects on the food supply, and economic effects compared to petroleum based plastic. Chemical Engineering, Worcester Polytechnic Institute. **Degree of Bachelor Science**: 58.

Moran, J. I., V. A. Alvarez, et al. (2008). "Extraction of cellulose and preparation of nanocellulose from sisal fibers." Cellulose **15**(1): 149-159.

Muszyński, L. and M. E. Launey (2010). "Advanced imaging techniques in wood-based panels research. in: Wood-Based Panels - An Introduction for Specialists. State-of-the-Art in Wood-Based Panels Research." COST Action E49: 177-201.

Nakagaito, A. N. and H. Yano (2004). "The effect of morphological changes from pulp fiber toward nano-scale fibrillated cellulose on the mechanical properties of high-strength plant fiber based composites." Applied physics A **78**(4): 547-552.

Nishino, T., K. Takano, et al. (1995). "Elastic modulus of the crystalline regions of cellulose polymorphs." Journal of Polymer Science:Part B: Polymer Physics **33**: 1647-1651.

Oksman, K., A. P. Mathew, et al. (2006). "Manufacturing process of cellulose whiskers/poly(lactic acid) nanocomposites." Composites Sci. Technol. **66**(15): 2776-2784.

Oksman, K. and M. Sain (2006). Cellulose nanocomposites-processing, characterization and properties. American Chemical Society. Washington, DC.

Paakko, M., M. Ankerfors, et al. (2007). "Enzymatic hydrolysis combined with mechanical shearing and high pressure homogenization for nanoscale cellulose fibrils and strong gels." Biomacromolecules **8**: 1934-1941.

Peng, S. and J. Zhang (2007). Engineering geology for underground rocks. Berlin Heidelberg, Springer.

Petersson, L., I. Kvien, et al. (2007). "Structure and thermal properties of poly(lactic acid)/cellulose whiskers nanocomposite materials." Composites Science and Technology **67**: 2535-2544.

Petersson, L. and K. Oksman (2006). Preparation and Properties of Biopolymer-Based Nanocomposite Film Using Microcrystalline Cellulose. American Chemical Society. Washington D.C: 132-151.

PolyOne. (2008). "White Paper: Biomaterials in the Polymer Industry." Retrieved August 5, 2011, from <http://www.polyone.com/en-us/docs/>.

Saleemi, A. S. and J. A. Nairn (1990). "The plane-strain essential work of fracture as a measure of the fracture toughness of ductile polymers." Polymer Engineering and Science **30**(4): 211-218.

- Sehaqui, H., M. Allais, et al. (2010). "Wood cellulose biocomposites with fibrous structures at micro- and nanoscale." Composites Science and Technology **71**(3): 382-387.
- Selomulya, C. (2001). The effect of shear on flocculation and floc size/structure. Chemical Engineering. **PhD**: 226.
- Siró, I. and D. Plackett (2010). "Microfibrillated cellulose and new nanocomposite materials: a review " Cellulose.
- Sun-Young, L., D. J. Mohan, et al. (2009). "Nanocellulose reinforced PVA composite films: effects of acid treatment and filler loading." Fibers and Polymers **10**(1): 77-82.
- Suryanegara, L., A. N. Nakagaito, et al. (2009). "The effect of crystallization of PLA on the thermal and mechanical properties of microfibrillated cellulose-reinforced PLA composites." Composites Science and Technology **69**: 1187-1192.
- Svagan, A. J., M. A. S. A. Samir, et al. (2007). "Biomimetic polysaccharide nanocomposites of high cellulose content and high toughness." Biomacromol. **8**(8): 2556-2563.
- Witzke, D. R. (1997). Introduction to Properties, Engineering, and Prospects of Polylactide Polymer. Chemical Engineering, Michigan State University. **Ph. D.**
- Wu, J. and Y.-W. Mai (1996). "The essential fracture work concept for toughness measurement of ductile polymers." Polymer Engineering and Science **36**(18): 2275-2288.
- Wu, Q., M. Henriksson, et al. (2007). "A High Strength Nanocomposite Based On Microcrystalline Cellulose and Polyurethane." Biomacromolecules **8**: 3687-3692.
- Zimmermann, T., E. Pohler, et al. (2004). "Cellulose fibrils for polymer reinforcement." Advanced Engineering Materials **6**(9): 754-761.
- Zimmermann, T., E. PÖHLER, et al. (2006). "Cellulose Fibrils: Isolation, Characterization, and Capability for Technical Applications." A.C.S. symposium series **938**: 33-47.

APPENDICES

Appendix A: DIC Setup and Working Procedures

The procedure consists of three major stages: the equipment setup and calibration, image acquisition, data processing. Below a step by step procedure for the first two stages is described.

1. Select and install proper lenses
 - a. inspect lenses for dust, smudges etc. (remove with an optical quality tissue)
 - b. carefully install the lenses on the cameras; do not force the positioning screws
 - c. connect cameras to the system:
 - i. connect the FireWire hub to the PC
 - ii. connect the FireWire cables to the hub
 - iii. connect the power source to the hub
 - iv. connect the trigger box cables to the cameras; check the LEDs on the back of the cameras – they should indicate the power, and trigger signals
 - v. report problems immediately.
 - d. Open VicSnap and check if the cameras work with the software
2. If the cameras work all right set up the unit #1 in front of the testing scene in such a way that all specimens are visible

3. Post warnings on the system perimeter e.g. “Experiment in progress, please do not turn off the lights, contact XX” give the beginning and end time for the measurement.

(for the next couple of steps keep at least one specimen in the testing position)

4. Once you have both cameras sending the signal figure out the position of the tripod so that the field of view covers all specimens (use one camera as a guide) and the tripod arm is parallel to the specimens plane;
 - a. extend the legs of the tripod so that the column is in a vertical position and the tripod has a comfortable wide base;
 - b. adjust the height of the tripod column, so that the cameras are at the level of half of the specimen height (you may need to release the screw securing the column first; remember to tighten the screw once the column height is set)
5. Adjust the position of the cameras on the bar:
 - a. first the distance between the cameras
 - b. second the level of the cameras: select a horizontal line in the field of view, which is visible in both camera windows and adjust the cameras until the line is at the same relative height in both windows
 - c. third the angle between the cameras: DO NOT FORCE THE ANGULAR POSITION of the cameras! Use the small Allen wrench to release two of the four mounting screws in the camera base, adjust the angle, hold the camera and tighten the screws again; the angular position of the

cameras should be such, that you see exactly the same field of view in both cameras

d. repeat steps a-c as needed

6. Set preliminary focus and micro-adjust the tripod
7. Set up the lights so that there is no reflection in the front plexi shield visible in neither of the camera windows, and so that the specimen surface looks more or less the same in both camera windows (you should be able to identify the same neighbourhoods on the speckled surface)

Note: check if the ambient light would not be sufficient;

8. Setting the camera focus (if the wide angle lenses are used you will need to release the mounting screw on the lenses to turn the dial and carefully tighten it to set the dial position; consult experienced users when in doubts):
 - a. Open the aperture all the way
 - b. Adjust the exposure time so that there is no saturated (red) area on the specimens
 - c. Enlarge the camera window to the point where you see the pixels, and make the speckled surface fill the screen
 - d. Adjust focus moving the focus dial back and forth couple times until you are convinced you are in the right position
 - e. Step the aperture down to about 5.6 and adjust the exposure time until there is no saturated (red) area on the specimens (saturated area in the back ground is OK)

9. Repeat with the other camera.
10. Remove the specimens from the field of view and calibrate the cameras using the largest target that fits in the field of view.
 - a. If you plan to shoot through a glass between the cameras and the specimen, calibrate with the front glass on! You may need another person to snap the images for you.
 - b. Follow the steps described in the user manual;
 - c. Take about 24 images for each calibration.
 - d. Whenever possible rest the target on the base or hold it against a firm base (this increases your chance for successful calibration)
 - e. Remember to save each calibration in a separate file after the calibration is accepted.
 - f. Take at least two calibrations (if the calibrations go smooth; take more if you experience problems or are unsure about the result; save all calibrations) and then chart down all the calibration parameters in an excel file
11. Install one specimen
12. In vicSnap Initiate a new project, and snap about 5 images
13. Move to vic3D:
 - a. initiate a new project,
 - b. import the best calibration
 - c. select an area of interest on the specimen

- d. try calculations with the default subset size and step
- e. If there is too much error try placing the start point (the yellow crossed box) in a different place or reducing the subset size (however it should not be less than 9)
- f. if this does not help try gradually enlarging the subset size (but no more than 31) while enlarging the subset step to about half the subset size
- g. If this does not help try changing the lighting position slightly
- h. if still in trouble try importing another calibration file
- i. if this still does not help call on an experienced operator for assistance

14. Once the calculation goes smooth:

- a. Install all specimens
- b. Repeat steps 10 and 11 with all specimens adding areas of interest only when you get the calculations smooth with the previous one. You need to have a decent area of interest on each of the specimens.

15. Once calculation goes smooth for all areas of interest, use “export statistics”

to save a csv file with means and standard deviations for all specimens;

16. Return to vicSnap and set up the image acquisition schedule: the frequency

may be set up from 5 frames per second to one image per day or longer. NOTE: make sure you set the running time, otherwise the image acquisition will stop at the default time, which may be just couple hours from start, and the rest of the data will be lost).

While the image acquisition is pending you may move to Vic3D and start calculations.

This may let you detect unexpected problems with your setup early.

Appendix B—Equivalence of Equations (9) and Equation (10)

Symbols:

w_t - area under entire stress-strain curve (specific work to failure), [J/m³]

w_t^p - area under entire stress-strain curve (specific work to failure) for a point, [J/m³]

w_e^* - essential work of fracture per volume, area of the triangle [J/m³]

w_e^{*p} - essential work of fracture per volume, area of the triangle [J/m³]

w_p - specific work of plastic deformation [J/m³]

W_T - total work to failure, [J]

W_p - total work for plastic deformation, [J]

W_p^p - total work of plastic deformation for a point, [J]

w_p^p - specific work of plastic deformation for a point, [J/m³]

ΔA - area of subset (point) , [m²]

A - area of AOI, [m²]

l - ligament length, [m]

t - thickness of specimen, [m]

Starting from individual points:

$$w_p^p = \frac{W_p^p}{\Delta A t} = w_t^p - w_e^{*p}$$

$$W_p^p = (w_t^p - w_e^{*p})\Delta A t$$

Then the total work of plastic deformation for entire sample will be:

$$W_p = \sum_A W_p^p = \Delta A t \sum_A w_p^p \quad (\text{B1})$$

Where

n is the number of points in the entire AOI.

Starting from mean strains:

$$\bar{w}_p = \frac{\bar{W}_p}{A t} = \bar{w}_t - \bar{w}_e^*$$

Where the bars indicate values calculated from the mean strains-stress curve

$$\bar{w}_t = \frac{\bar{W}_t}{A t} = \sum_{\text{time}} \bar{\sigma} \Delta \bar{\varepsilon}$$

$$\Delta \bar{\varepsilon} = \bar{\varepsilon}_{i+1} - \bar{\varepsilon}_i = \frac{1}{n} \left(\sum_A \varepsilon_{i+1} - \sum_A \varepsilon_i \right) = \frac{1}{n} \sum_A \Delta \varepsilon$$

Then

$$\bar{w}_t = \frac{\bar{W}_T}{A t} = \sum_t \bar{\sigma} \Delta \bar{\varepsilon} = \sum_t \bar{\sigma} \left(\frac{1}{n} \sum_A \Delta \varepsilon \right) = \frac{1}{n} \sum_t \left(\sum_A \bar{\sigma} \Delta \varepsilon \right) = \frac{1}{n} \sum_A \left(\sum_t \bar{\sigma} \Delta \varepsilon \right)$$

$$\bar{w}_t = \frac{\bar{W}_T}{A t} = \frac{1}{n} \sum_A w_t^p$$

and

$$\bar{w}_e^* = 0.5 \bar{\sigma}_{\max \varepsilon} (\bar{\varepsilon}_{\max} - \bar{\varepsilon}_p) = 0.5 \bar{\sigma}_{\max \varepsilon} \frac{1}{n} \sum_A (\varepsilon_{\max} - \varepsilon_p)$$

$$= \frac{1}{n} \sum_A 0.5 \bar{\sigma}_{\max \varepsilon} (\varepsilon_{\max} - \varepsilon_p)$$

$$\bar{w}_e^* = 0.5 \bar{\sigma}_{\max \varepsilon} (\bar{\varepsilon}_{\max} - \bar{\varepsilon}_p) = \frac{1}{n} \sum_A w_e^{*p} \quad (\text{B2})$$

Substitute

$$\bar{w}_p = \frac{\bar{W}_p}{At} = \bar{w}_t - \bar{w}_e^* = \frac{1}{n} \sum_A w_t^p - \frac{1}{n} \sum_A \bar{w}_e^* = \frac{1}{n} \sum_A (w_t^p - \bar{w}_e^*) = \frac{1}{n} \sum_A w_p^p$$

$$\bar{W}_p = (\bar{w}_t - \bar{w}_e^*)At = \frac{At}{n} \sum_A w_p^p = \Delta At \sum_A w_p^p$$

Compared to equation (B1), it indicates that the total work of plastic deformation in a sample calculated from two methods are equivalent.

Then the essential work of fracture may be approximated from the diagrams of nominal stress and average sample strain:

$$w_e = \bar{w}_e^* \frac{A}{l} = 0.5 \bar{\sigma}_{max\epsilon} (\bar{\epsilon}_{max} - \bar{\epsilon}_l) \frac{A}{l}$$

Appendix C—Matlab Codes for EWF Computation

```

%script twpd_meaneyy_LM02
% modified by Lech 8/19/2011
% modified by Lech 8/22/2011
% modified by Jie 8/26/2011

clear;
clear all;

% read meaneyy and force for stress calculation
meaneyy= xlsread('09_stats','z2:z97');

% Note that the force and position in file a1 start from non-zero
valules.
% Note also, that the raw position is not the same as displacement.
% Either the specimens were pre-stressed or the machine was not
balanced
% for zero-force before testing
%Let's assume that the force offset is small enough to be ignored (1%
of
%the max value) and the displacement may be calculated from the x-
head
%positon by subtracting the initial value
in_dir = 'C:\Users\dingj\Desktop\matlab temp folder\Mat_09\';
force_raw = xlsread('09','g2:g97');
position_raw = xlsread('09','f2:f97');

force = force_raw - force_raw(1);
disp = position_raw - position_raw(1);

%Plot force-displacement diagtam from Instron data recorded by DIC
figure(1);
subplot(1,2,1); plot(disp,force);
title({'force-displacement diagram'; '(based on Instron X-head
position)'})
xlabel('displacement, mm')
ylabel('force, N')
%axis([0 ceil(max(disp)) 0 ceil(max(force))])
axis([-0.1 1.5 -10 100])
axis square
grid on

% step size in pixels
ss_p = 5; % pixels

% spatial resolution mm/pixel
sr = 25/565; %provide a solid number here

% specimen width in mm [provide actual specimen width]
w=0; %[provide actual specimen width]

```

```

% specimen length in mm [provide actual specimen gauge length]
h=75;    %[provide actual specimen gauge length] then text the steps
for
    % calculating the dimensions of the AOI

% specimen thickness in mm
t=0.1; % mm

% ligament length of the specimen in mm
l=3.4; % mm

% calculate the area of AOI in mm2
%%%%%%%%%%%%%%%%%%%%%%%%%%%%%%%%%%%%%%%%%%%%%%%%%%%%%%%%%%%%%%%%%%%%%%%%
%in_dir = 'C:\Users\dingj\Desktop\matlab temp folder\Mat_a2\';
listing = dir([in_dir, '*.mat']);
no_files = length(listing); % count number of files
% read sizes of eyy and eyy_0 matrices
load([in_dir, listing(1).name], 'eyy', 'eyy_0');

% calculate the number of subareas (dA) in the AOI that are not NaN
ndA= sum(~isnan(eyy_0(:)))+ sum(~isnan(eyy(:)));

% elementary area
dA = (ss_p*sr)^2;

%The area of AOI
A = ndA*dA;

%stress vector
syy = force/(l*t);

%Plot stress-strain diagram with strains from optical measurement
subplot(1,2,2); plot(meaneyy, syy)
title({'stress-strain diagram'; '(based on DIC mean strains)'})
xlabel('strain (DIC), mm/mm')
ylabel('stress, MPa')
%axis([0 ceil(max(meaneyy))/100 0 ceil(max(syy))])
axis([-0.001 0.01 -10 120])
axis square
grid on

% find the position of stress at maximum eyy
[meaneyy_max, I]=max(meaneyy);

figure(1); subplot(1,2,2); hold on;
plot(meaneyy(I), syy(I), 'rs')
plot(meaneyy(end), syy(end), 'ro')

%calculate area under stress-stain curve

```

```

dmeaneyy = diff(meaneyy);
isyy = (syy(1:end-1)+ syy(2:end))/2;

%sum only up to eyy max (less one because of the differentiation)
swd = sum(isyy(1:I-1).*dmeaneyy(1:I-1));

% Calculate the work of plastic deformation in J/m^3
%swp = swd - swf;
swp = sum(isyy.*dmeaneyy);

% total work of plastic deformation in J

%twpd = t*A swp

%compare to the complete area under the stress-strain curve
twpd = sum(isyy.*dmeaneyy)*A*t

%%%%%%%%%%%%%%%%%%%%%%%%%%%%%%%%%%%%%%%%%%%%%%%%%%%%%%%%%%%%%%%%%%%%%%%%
% essential work of fracture
% ewf = swf*A/l
ewf = (swd-swp)*A/l

%compare

ewf_s = -sum(isyy(I:end).*dmeaneyy(I:end))*A/l

%%%%%%%%%%%%%%%%%%%%%%%%%%%%%%%%%%%%%%%%%%%%%%%%%%%%%%%%%%%%%%%%%%%%%%%%
% calculate total work to failure from force-displacement curve
disp = disp - disp(1);

% step 1: calculate displacement differentials
ddisp = diff(disp);

% step 2: interpolate the step mean values for force
iforce = (force(1:end-1)+ force(2:end))/2;

% step 3: "integrate" along displacement axis, the result is the area
under
% the force-displacement curve, i.e., total work to failure

work_tot = sum(ddisp(1:I-1).*iforce(1:I-1))
work_tt = sum(ddisp.*iforce)

%compare to area under stress-stain curve multiplied by volume
work_tot_s = swd*A*t

```

Appendix D—SEM Micrographs of MFC Aerogel Samples

There are two folders in this CD. Each folder contains SEM micrographs of one type of MFC aerogel.

1. Folder labeled "UMaine MFC aerogel" contains SEM micrographs of MFC from University of Maine (referred as type A MFC in the thesis). Two pieces of leaf-like flakes at different locations were cut by Focused Ion Beam (FIB) in order to observe the internal structure of the flakes. There are two folders under this folder.

➤ Folder "FIB_01 ": a series of SEM micrographs of FIB-cut flake at different magnification levels:

- CL_MFC FIB_100x
- CL_MFC FIB_800x
- CL_MFC FIB_1 500x
- CL_MFC FIB_6 500x
- CL_MFC FIB_20 000x
- CL_MFC FIB_35 000x
- CL_MFC FIB_50 000x

➤ Folder "FIB_02 ": another series of SEM micrographs of FIB-cut flake at various magnification levels:

- CL_MFC FIB_100x
- CL_MFC FIB_800x
- CL_MFC FIB_5 000x

- CL_MFC FIB_15 000x
- CL_MFC FIB_20 000x
- CL_MFC FIB_35 000x
- CL_MFC FIB_50 000x

2. Folder labeled "Swedish MFC aerogel" contains SEM micrographs of MFC from Innventia AB company, Sweden (referred as type B MFC in the thesis). There is a series of SEM micrographs of type B MFC aerogel at various magnification levels in this folder:

- MFC_Sweden_1 000x
- MFC_Sweden_10 000x
- MFC_Sweden_15 000x
- MFC_Sweden_20 000x
- MFC_Sweden_25 000x
- MFC_Sweden_50 000x
- MFC_Sweden_65 000x
- MFC_Sweden_150 000x
- MFC_Sweden_200 000x